Journal of Energy Storage 165 (2026) 122298

Contents lists available at ScienceDirect

Journal of Energy Storage

journal homepage: www.elsevier.com/locate/est

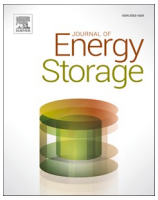

Research papers

# Novel multi-lobed tube designs for efficient latent thermal energy storage: A comprehensive study of single and dual-tube configurations

Mhamed Benaissa [a], Nashmi H. Alrasheedi [b,*], Jasim M. Mahdi [c], Hayder I. Mohammed [d], Khalil Hajlaoui [b], Mehdi Ghalambaz [e,*], Mehdi Fteiti [f], Nidhal Ben Khedher [g]

[a] Department of Chemical Engineering, University of Ha'il, Ha'il, Saudi Arabia
[b] College of Engineering, Imam Mohammad Ibn Saud Islamic University (IMSIU), Riyadh, Saudi Arabia
[c] Center of Excellence in Renewable Energy, University of Baghdad, Baghdad 10071, Iraq
[d] Department of Cooling and Air Conditioning Engineering, Imam Ja'afar Al-Sadiq University, Baghdad, Iraq
[e] Department of Mathematical Sciences, Saveetha School of Engineering, SIMATS, Chennai, India
[f] Physics Department, Faculty of Science, Umm Al-Qura University, Makkah, 24381, Saudi Arabia
[g] Department of Mechanical Engineering, University of Ha'il, Ha'il, Saudi Arabia

ARTICLE INFO

*Keywords:*
Phase change material
Thermal energy storage
Geometric modification
Multi-lobed tube
Dual-tube configuration

ABSTRACT

Low thermal response of phase change materials (PCMs) severely restricts the viability of latent thermal energy storage (LHTES) systems. Unlike conventional fin-based enhancement methods that add external structures and reduce PCM volume, this study explores geometric modification of the heat transfer tube cross-section itself to maintain full storage capacity while optimizing thermal interaction through tube shape alone. Nine configurations were numerically analyzed using validated numerical modeling: single-tube multi-lobed designs (4-lobe, 6-lobe, 8-lobe), extended lobe configurations (10–15 mm extensions), and novel dual-tube connected systems with intermediate thermal zones. Both charging and discharging modes were evaluated under medium-temperature conditions. The optimal single-tube configuration (8-lobe, 15 mm extensions) achieved heat storage and release rates of 194.70 W and 189.16 W, representing 87% and 175% improvements over baseline circular design. Most significantly, the dual-tube connected configuration (60 mm secondary diameter) achieved exceptional performance: 303.73 W storage and 401.54 W release rates producing 192% and 484% enhancements over baseline. Complete melting and solidification times were reduced by 35% and 54% respectively versus optimal single-tube design. Results establish clear guidelines: optimal lobe densities of 6–8 and secondary tube diameters of 60–70 mm provide maximum enhancement for practical implementation.

## 1. Introduction

The global transition toward renewable energy sources has created an urgent need for efficient thermal energy storage (TES) systems that can bridge the temporal gap between energy supply and demand [1,2]. Phase change materials (PCMs) have emerged as particularly promising candidates for this application due to their ability to store and release substantial amounts of thermal energy during their isothermal phase transitions [3]. However, the widespread adoption of PCM-based latent TES (LHTES) faces a fundamental limitation: the inherently low thermal conductivity of most PCMs significantly restricts heat transfer rates and prolongs charging and discharging cycles [4]. Typically, organic PCMs have the thermal conductivity (up to 0.2 W/m K), followed by inorganic PCMs (0.2–0.8 W/m K) [5]. These limitations directly impact the economic viability and operational effectiveness of PCM-based TES systems, as they reduce power density and require larger system volumes to achieve desired performance levels [6].

The recognition of low thermal conductivity as the primary barrier to PCM technology adoption has motivated extensive research into heat transfer enhancement methods [7]. Enhancement methods can be categorized into three fundamentally different approaches: (1) material modification through additives [8–10], (2) external augmentation via fins or foams [11,12], and (3) geometric optimization of the HTF containment structure itself [13,14]. The material modification through additives frequently alters the fundamental thermophysical properties of the PCM, potentially affecting its phase change temperature, latent

* Corresponding authors.
*E-mail addresses:* nhrasheedi@imamu.edu.sa (N.H. Alrasheedi), ghalambaz.mehdi@gmail.com (M. Ghalambaz).

https://doi.org/10.1016/j.est.2026.122298
Received 29 November 2025; Received in revised form 4 April 2026; Accepted 17 April 2026
Available online 24 April 2026
2352-152X/

heat capacity, and long-term stability. External augmentation methods, while preserving PCM properties, typically require additional materials and manufacturing steps that increase system costs and complexity [15]. Recent studies suggest optimizing fin spacing and inclination angles [16] to enhance PCM system efficiency without substantially compromising storage volume [17–19]. Meanwhile, geometric modification of the HTF tube cross-section, the focus of this study, can enhance thermal performance without adding materials or reducing PCM volume. By reshaping the tube itself from circular to multi-lobed configurations, heat transfer surface area increases while maintaining 100% PCM storage capacity. This approach represents a new different enhancement philosophy: optimizing the thermal interaction geometry rather than adding heat transfer augmentation structures.

Structural modifications typically represent a crucial approach for enhancing heat transfer phenomena in LHTES applications [20,21]. The configuration of PCM containment vessels directly influences convective flow patterns within the phase change medium, thereby affecting overall heat transfer performance [22]. Research by Khedher et al. [23] examined various geometric parameters of PCM containers in vertical latent heat double-pipe heat exchangers and their impact on thermal charging behaviour. Their investigation revealed that implementing a smooth framed configuration could decrease melting duration by 55% while boosting thermal energy storage rates by 115% relative to unframed designs. Similarly, Pahamli et al. [24] demonstrated that repositioning the inner tube within double-pipe heat exchangers promotes natural convection enhancement. Their work showed that displacing the inner tube containing RT-50 phase change material expanded the heat transfer surface area, resulting in a 64% reduction in melting duration. Seddegh et al. [25] analyzed four distinct radius ratios in shell-and-tube heat exchanger configurations, observing that increasing the shell-to-tube radius ratio corresponded with decreased PCM melting times. Ye et al. [26] investigated how different geometric parameters of PCM containers including elbow radius, radial eccentricity, and inclination angle can influence melting behaviour in L-shaped shell-and-tube LHTES configurations. Their results demonstrated that enhanced radial eccentricity substantially improved heat transfer by increasing PCM exposure to natural convection effects, whereas elbow radius variations showed minimal impact. Włoszyń et al. [27] examined shell shape influences on LHTES system charging and discharging rates, finding that a downward-positioned semi-circular shell configuration achieved the briefest melting time, 44% faster than the reference circular design, while an upward-oriented isosceles trapezium demonstrated the shortest solidification period.

Beyond conventional configurations, researchers investigated complex non-circular pipe geometries as a promising direction in geometric optimization research. NematpourKeshteli et al. [28] examined lobed double-pipe configurations, demonstrating 18.32% and 11.40% reductions in charging and discharging times with six-lobed surfaces. Extending these concepts, Najafabadi et al. [29] examined twisted double-pipe heat exchangers featuring lobed cross-sections. Their research revealed that a 3-lobed cross-section improved PCM melting by 6% over circular cross-sections, confirming the effectiveness of multi-lobed geometric modifications. Najababadi et al. [30] studied double-pipe helical coil LHTES systems incorporating Koch snowflake cross-sections for melting enhancement. Their analysis revealed that increased helical pitch improved melting rates by 3.2%, while larger coil diameters had adverse effects on melting performance. However, all of these prior studies employ geometrically modified tubes as single, self-contained HTF conduits without extending HTF pathways into the PCM domain through physically connected network. Table 1 summarizes how the present dual-tube connected configuration differs from three established multi-tube LHTES designs, demonstrating that the present design is distinguished by a fundamentally different heat transfer topology: a single interconnected HTF network delivering multi-directional thermal penetration through physically connected fluid bridges, an architectural feature absent in all three reference classes.

**Table 1**
Comparative classification of multi-tube PCM thermal storage configurations.

| Feature | Triplex-tube (e.g., Al-Abidi et al.) | Multi-pipe / shell-and-multitube | Cascaded dual-PCM systems | Present dual-tube connected configuration |
|---|---|---|---|---|
| Number of independent HTF streams | 2 (inner + outer annulus) | Multiple parallel pipes | 2 (separate PCM stages) | 1 (single interconnected network) |
| Heat transfer pathway topology | Parallel (PCM between two HTF streams) | Parallel | Series (two PCM materials, staged) | Series geometric cascade through single PCM via intermediate fluid-carrying lobed bridges |
| PCM | Single or dual | Single | Typically two different PCMs | Single PCM |
| Enhancement mechanism | Surface area extension + dual-side heating | Surface area extension | Thermal staging via PCM properties | Geometric partitioning of PCM domain into thermally cascaded zones via connected HTF network |
| Physical connection between tubes | None (separate flow circuits) | None | None | Fluid thermal bridges (lobed connections) |

The present study systematically evaluates single-tube and dual-tube configurations featuring various multi-lobed cross-sections in shell-and-tube PCM storage systems, covering both melting and solidification processes under convective boundary conditions representative of medium-temperature thermal storage applications (60 °C/30 °C for melting, 40 °C/10 °C for solidification). The introduction of connected dual-tube configurations with intermediate thermal zones represents a novel approach to PCM thermal storage design that has not been previously investigated in the literature. The findings provide fundamental insights into heat transfer enhancement mechanisms in PCM systems. The comprehensive comparison framework establishes performance benchmarks and design guidelines that can inform future research and development efforts.

## 2. Problem statement and system description

A horizontal LHTES system consists of a cylindrical shell-and-tube arrangement is investigated in this study. The system maintains a constant PCM volume across all geometric configurations to ensure useful performance comparisons. The outer cylindrical shell features adiabatic boundary conditions. The inner tube serves as the primary heat transfer interface, with the HTF (water) flowing through the modified cross-sectional geometries at controlled inlet temperatures and flow rates. As shown in Fig. 1 and Table 2, the baseline configuration (Case 1) features a standard circular tube with an internal diameter of 40 mm, establishing the reference case for all performance evaluations. The tube wall thickness is maintained at 2 mm across all configurations to ensure structural integrity while minimizing thermal resistance through the tube material.

The single-tube modifications progress from 4-lobe to 8-lobe configurations, with each design optimized to maximize heat transfer surface area. The 4-lobe design (Case 2) features four symmetrical radial lobes positioned at 90° intervals, with each lobe extending 10 mm into the PCM domain. The lobe width tapers from 27.25 mm at the base to maintain structural continuity with the central tube. The 6-lobe design (Case 3) incorporates six symmetrical lobes at 60° intervals, creating a star-like pattern that provides more uniform thermal field distribution.

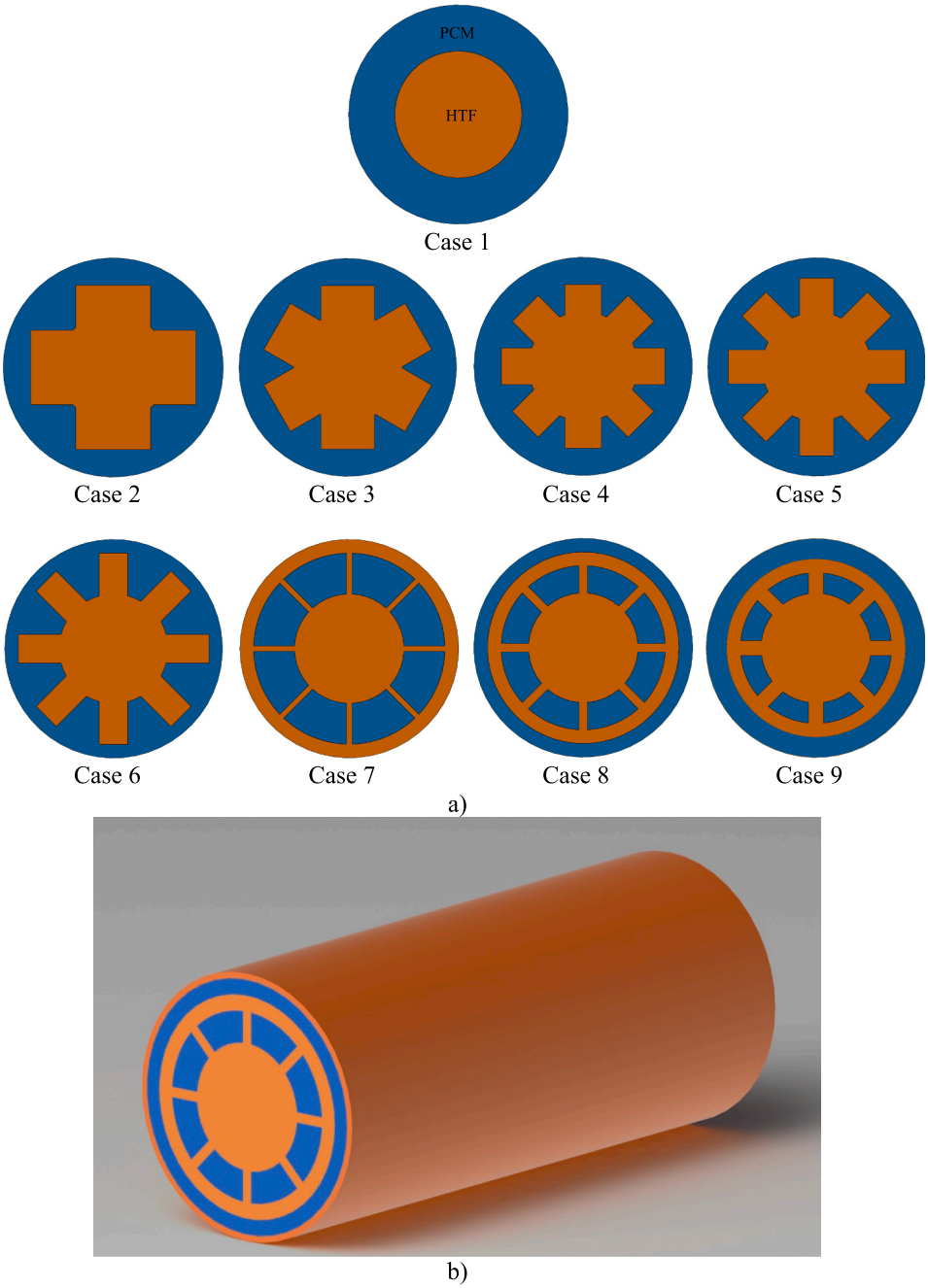


**Fig. 1.** a) Cross-sectional geometries of single-tube configurations (Cases 1–6) and dual-tube configurations (Cases 7–9) and b) 3D view of case 8.

The reduced angular spacing allows for lobe widths of 19.6 mm while maintaining the same 10 mm extension length. The 8-lobe design (Case 4) represents the maximum number of lobes achievable while maintaining adequate structural support between adjacent extensions. The eight lobes, positioned at 45° intervals with 15.18 mm base width. Extended configurations (Cases 5–6) explore the effects of increased radial penetration into the PCM domain. The Extended 8-lobe design (Case 5) features 12.5 mm lobe extensions with reduced base widths of 12.41 mm, while the Deep-extension design (Case 6) maximizes PCM engagement with 15 mm extensions and 10.45 mm base widths.

The dual-tube systems represent a paradigm shift in PCM thermal storage design, introducing intermediate thermal zones that create cascaded heat transfer pathways. These configurations combine the surface area benefits of multi-lobed geometries with the enhanced thermal distribution capabilities of nested tube arrangements. The dual-tube connected-lobe design (Case 7) features a primary 8-lobe inner tube connected to a secondary circular tube with a 70 mm internal diameter. The connection geometry creates a thermal bridge that allows heat to flow from the primary HTF stream through the lobed interface, into the intermediate PCM zone, and then through the secondary tube boundary. Optimized dual-tube systems (Cases 8–9) refine the dual-tube concept through systematic optimization of the secondary tube diameter and connection geometry. Case 8 features a 60 mm secondary tube diameter with shortened connection lengths to minimize thermal resistance, while Case 9 further reduces the secondary tube to 55 mm diameter with deep, compact connections that maximize thermal interaction density. Note that the 3D view of case 8 is also illustrated in Fig. 1b.

The investigation encompasses both charging (melting) and discharging (solidification) operations under conditions representative of medium-temperature thermal storage applications. The selected PCM is

**Table 2**
Specifications summary for the PCM thermal storage cases.

| Case | Name | Key parameters of the inner tubes | Secondary tube ID (mm) | Connection length (mm) | Shell ID (mm) |
|---|---|---|---|---|---|
| 1 | Baseline | Core ID: 40 mm, no modifications | – | – | 150 |
| 2 | 4-lobe design | Lobe width: 27.25 mm, length: 10 mm | – | – | 150 |
| 3 | 6-lobe design | Lobe width: 19.6 mm, length: 10 mm | – | – | 150 |
| 4 | 8-lobe design | Lobe width: 15.18 mm, length: 10 mm | – | – | 150 |
| 5 | Extended 8-lobe design | Lobe width: 12.41 mm, length: 12.5 mm | – | – | 150 |
| 6 | Deep-extension 8-lobe design | Lobe width: 10.45 mm, length: 15 mm | – | – | 150 |
| 7 | Dual-tube 8-lobe design | Primary: 8 lobes, core ID: 40 mm | 70 | 15 | 150 |
| 8 | Dual-tube 8-lobe design with shorter connection | Primary: 8 mini-lobes, core ID: 40 mm | 60 | 10 | 150 |
| 9 | Dual-tube 8-lobe design with deep shorter connection | Primary: 8 compact-lobes, core ID: 40 mm | 55 | 8 | 150 |

RT35 (Table 3). The charging process employs an HTF inlet temperature of 60 °C with initial PCM temperature of 30 °C, representing a 30 °C temperature differential that is characteristic of many practical thermal storage applications. The charging process continues until complete melting is achieved throughout the PCM domain. The discharging process utilizes an HTF inlet temperature of 10 °C with initial PCM temperature of 40 °C, creating a 30 °C temperature differential for solidification. The discharging process continues until complete solidification occurs, with particular attention to the effects of natural convection on the solidification pattern.

## 3. Mathematical modeling

### 3.1. Governing equations

The mathematical model incorporates several fundamental assumptions that reflect the physical nature of the system under investigation. The PCM density variation during phase change is explicitly accounted for through appropriate thermophysical properties, while natural convection effects are captured using the Boussinesq approximation. The heat transfer fluid flow is characterized as laminar, incompressible, and Newtonian, with temporal periodicity assumed for steady-state convergence. The system boundaries are considered adiabatic to isolate the performance enhancement effects of the geometric modifications, while viscous dissipation effects are neglected due to the relatively low Reynolds numbers encountered in typical TES applications. Under these theoretical considerations, the fundamental conservation equations governing mass, momentum, and energy transport are mathematically expressed through the following differential equations [32,33]:

**Table 3**
The nominal thermal properties of RT-35 [31].

| $\rho_l$ (kg/m$^3$) | $\rho_s$ (kg/m$^3$) | $k$ (W/m.K) | $C_p$ (J/kg K) | $\upsilon$ (m$^2$/s) | $\beta$ (K$^{-1}$) | $L$ (J/kg) | $T_l$ (°C) | $T_s$ (°C) |
|---|---|---|---|---|---|---|---|---|
| 770 | 880 | 0.2 | 2000 | $5 \times 10^{-6}$ | 0.00091 | 160,000 | 32 | 38 |

$$\frac{\partial \rho}{\partial t} + \nabla \cdot \rho \vec{V} = 0 \tag{1}$$

$$\rho \frac{\partial \vec{V}}{\partial t} + \rho\left(\vec{V} \cdot \nabla\right)\vec{V} = -\nabla P + \mu\left(\nabla^2 \vec{V}\right) - \rho_{ref}\beta\left(T - T_{ref}\right)\vec{g} - \vec{S} \tag{2}$$

$$\frac{\partial\left(\rho C_p T\right)}{\partial t} + \nabla \cdot \left(\rho C_p \vec{V} T\right) = \nabla \cdot (k \nabla T) - S_L \tag{3}$$

where $\rho$ is the PCM density (kg/m$^3$), $t$ is time (s), and V is the velocity vector (m/s), $P$ is the pressure (Pa), $\mu$ is the dynamic viscosity (Pa·s), $\beta$ is the thermal expansion coefficient (K$^{-1}$), $T$ is the local temperature (°C), $g$ is the gravitational acceleration vector (m/s$^2$), $C_p$ is the specific heat capacity (J/kg·K), and $k$ is the thermal conductivity. The Darcy-law momentum damping source term ($\vec{S}$) is defined as [34]:

$$\vec{S} = A_m \frac{(1-\lambda)^2}{\lambda^3 + 0.001}\vec{V} \tag{4}$$

The mushy zone constant ($A_m$) is assigned a value of ($10^5$) based on established literature recommendations [35–37], providing appropriate momentum damping in the partially solid regions while maintaining numerical stability. The small constant 0.001 is a regularization term that prevents division-by-zero singularity when $\lambda \to 0$ in fully solidified regions. It follows the standard enthalpy-porosity implementation practice [35–37]. Its influence on computed thermal performance metrics is negligible, as bulk quantities are governed by the thermal field. The liquid fraction parameter ($\lambda$) serves as the primary indicator of the local phase state, ranging from zero in the solid phase to unity in the liquid phase. This parameter is mathematically defined through the enthalpy-based formulation [35]:

$$\lambda = \frac{\Delta H}{L_f} = \begin{cases} 0 & \text{if } T < T_{\text{Solidus}} \\ \dfrac{T - T_{\text{Solidus}}}{T_{\text{Liquidus}} - T_{\text{Solidus}}} & \text{if } T_{\text{Solidus}} \le T \le T_{\text{Liquidus}} \\ 1 & \text{if } T > T_{\text{Liquidus}} \end{cases} \tag{5}$$

The latent heat source term ($S_L$) in the energy conservation equation represents the temporal and spatial variations in thermal energy associated with phase transformation processes:

$$S_L = \frac{\partial\left(\rho \lambda L_f\right)}{\partial t} + \nabla \cdot \left(\rho \vec{V} \lambda L_f\right) \tag{6}$$

This formulation consists of two distinct physical mechanisms: the temporal component $\partial\left(\rho\lambda L_f\right)/\partial t$ quantifies the rate of energy absorption or release due to local phase state changes, while the convective component $\left(\rho \vec{V} \lambda L_f\right)$ accounts for the transport of latent heat through liquid motion. During the melting process, the positive temporal derivative of ($\lambda$) creates a negative source term, representing the energy sink associated with solid-to-liquid transformation. Conversely, during solidification, the negative temporal derivative generates a positive source term, reflecting the latent heat release during liquid-to-solid crystallization.

The energy storage/release rate in the different multi-lobed tube configurations during the charging and discharging operations is mathematically estimated as:

$$\dot{E}_T = \frac{E_e - E_i}{t_p} \tag{7}$$

where ($t_p$) represents the characteristic time duration for complete melting or solidification, while ($E_e$) and ($E_i$) denote the total thermal energy content of the PCM at the conclusion and initiation of the respective process. The total energy content (E) encompasses both sensible heat contributions ($MC_pdT$) and latent heat contributions ($ML_f$), providing a comprehensive measure of the thermal storage capacity. During the charging phase, ($E_T$) quantifies the net rate of energy accumulation within the PCM, combining sensible heating effects and latent heat absorption during the solid-to-liquid transition. The discharging phase evaluation involves the assessment of energy release rates, incorporating both sensible cooling and latent heat liberation during liquid-to-solid freezing. This time-averaged formulation provides a consistent and practically relevant basis for comparing nine configurations across both melting and solidification modes, while transient behaviour and phase-change kinetics are complementarily captured through the liquid fraction and mean temperature evolution curves reported for all configurations in Section 5.

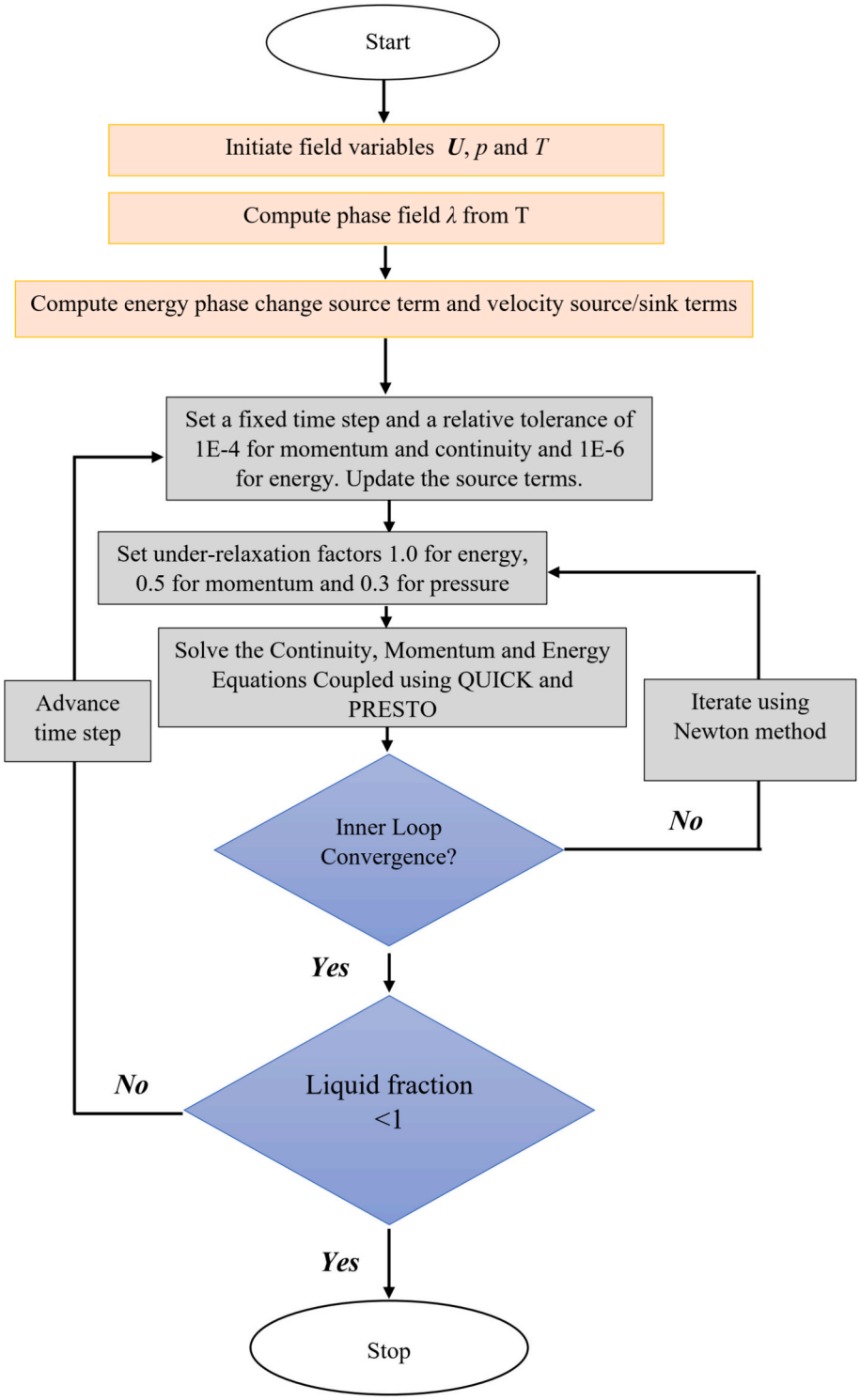


**Fig. 2.** Diagram of numerical code implementation for solving the governing equations.

### 3.2. Boundary and initial conditions

The thermal cycling operation consists of two distinct phases: charging (melting) and discharging (solidification), each characterized by specific temperature and thermal boundary conditions. The charging process commences with the entire PCM domain initialized at a uniform temperature of 30 °C, representing the initial solid-state condition. The primary heat transfer surface (multi-lobed tube) is maintained at a constant temperature of 60 °C, providing the thermal driving force for melting. Secondary heat transfer surfaces in dual-tube configurations are thermally insulated during this phase to prevent parasitic heat losses and ensure controlled energy input. Upon completion of the charging phase, the system transitions to the discharging operation with the PCM domain initialized at 40 °C in the liquid state. The thermal boundary conditions are reversed, with the primary heat transfer surface maintained at 10 °C to drive solidification, while previously active surfaces are thermally insulated. The laminar flow assumption is justified by the low Reynolds numbers characteristic of LHTES applications. For water flowing through the 40 mm primary tube at typical operating velocities of 0.01–0.05 m/s, $Re < 100$, well below the laminar-transitional threshold of 2300 [38]. This condition holds across all investigated configurations, including the dual-tube connected designs, where local geometric complexity influences boundary layer development but does not alter the bulk flow regime.

## 4. Solution methodology and validation

The governing equations were solved using ANSYS-FLUENT with a finite volume approach. The SIMPLE algorithm was implemented to handle pressure-velocity coupling, while the QUICK scheme was used to discretize momentum and energy equations for third-order accuracy in capturing the heat transfer/fluid flow patterns during the PCM phase transitions. The PRESTO scheme was selected to manage pressure corrections, particularly beneficial for complex multi-lobed geometries. Under-relaxation factors were set at 0.3 for pressure and velocity, 0.5 for liquid fraction, and 1.0 for energy. Convergence criteria were established at $10^{-4}$ for continuity and momentum equations, and $10^{-6}$ for energy equations. The flowchart of the numerical method implementation is illustrated in Fig. 2.

Mesh independence tests were conducted on Case 8 using structured quadrilateral elements in both the HTF domain and the PCM region. Four mesh densities were examined: 100 K, 150 K, 200 K, and 300 K elements. As shown in Fig. 3a, liquid fraction predictions vary less than 0.5% between the 200 K and 300 K meshes in both melting and solidification, confirming grid-independent solutions. The 200 K mesh was therefore selected for all simulations, providing an optimal balance between accuracy and computational cost. Timestep sensitivity analysis examined intervals of 0.1, 0.2, and 0.4 s. Fig. 3b demonstrates that the 0.2 s timestep produces results within 0.5% of the 0.1 s solution while maintaining computational efficiency. A timestep of 0.2 s was therefore adopted for all simulations. Case 8 was selected for mesh independence testing as it represents the most geometrically complex configuration, featuring the smallest connection lengths and highest interface density among all dual-tube designs. Grid independence demonstrated for this case is therefore conservative when applied to simpler single-tube configurations, whose larger geometric features produce less severe local gradients.

Numerical predictions were validated against experimental data from Al-Abidi et al. [39] for a finned triplex-tube system with similar PCM thermophysical properties and comparable thermal boundary conditions. The experimental setup employed calibrated thermocouples with ±0.5% accuracy positioned at strategic locations throughout the PCM domain to capture both the temporal evolution of local temperatures and the spatial progression of the phase change front. Fig. 4 presents comparisons for both charging (Fig. 4a) and discharging (Fig. 4b) phases. The experimental thermocouples had ±0.5% accuracy. Maximum deviations remained below 3% during melting, with excellent agreement across initial sensible heating, isothermal phase change, and final superheating phases. Solidification validation successfully captured the heat transfer kinetics, with slight deviations during intermediate solidification. This validation approach therefore provides a reliable foundation for predicting thermal behaviour in multi-lobed configurations, establishing the credibility necessary for drawing meaningful conclusions about optimal geometric configurations and heat transfer enhancement mechanisms.

## 5. Results and discussion

### 5.1. Melting performance analysis

#### 5.1.1. Single-tube multi-lobed configurations

This section examines Cases 1–4, comparing the baseline circular tube with 4-lobe, 6-lobe, and 8-lobe designs. The baseline circular tube configuration (Case 1) serves as the reference against which the 4-lobe (Case 2), 6-lobe (Case 3), and 8-lobe (Case 4) designs are evaluated during the PCM melting process. The liquid-fraction evolution contour maps, as illustrated in Fig. 5, reveal fundamental differences in melting progression patterns between the circular and multi-lobed geometries. The baseline configuration exhibits radially symmetric melting that progresses slowly outward from the circular boundary, with the melting front maintaining a relatively uniform circular profile throughout the melting duration. In contrast, the multi-lobed configurations create multiple thermal penetration pathways that accelerate melting along preferential pathways corresponding to each lobe extension.

At the initial 600-s interval, the lobed geometries demonstrate localized melting initiation at each lobe tip, forming distinct thermal

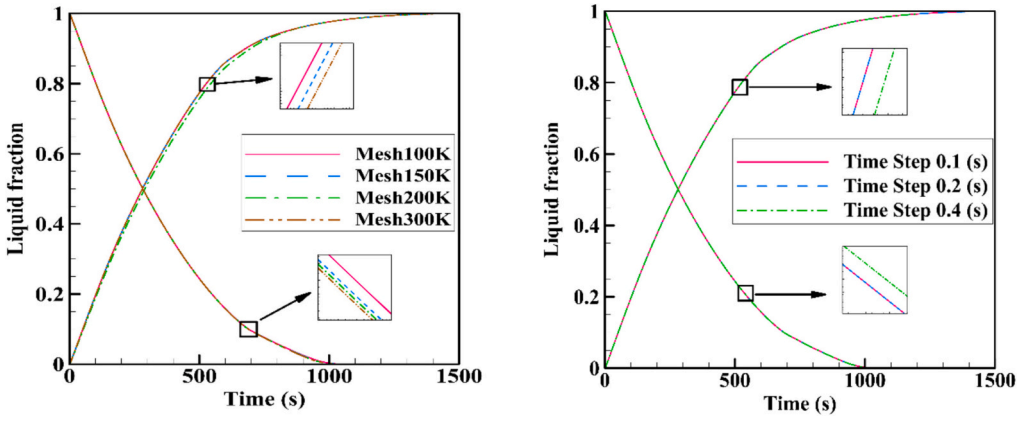


**Fig. 3.** Exploring the impact of a) the mesh size and b) the timestep size on the average temperature of the PCM during the melting phase.

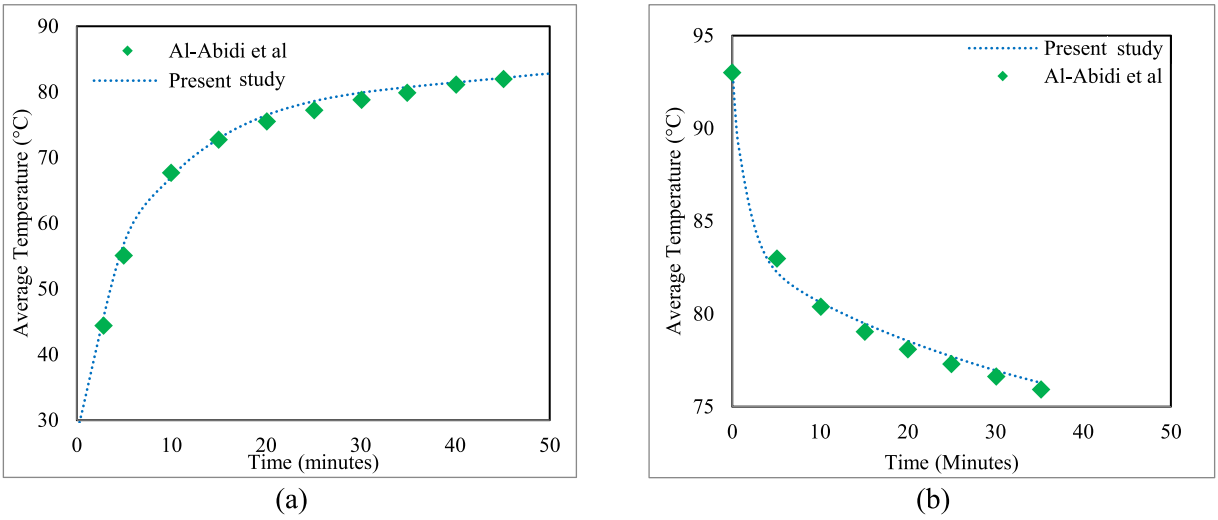


**Fig. 4.** Model validation over the charging phase (a) and the discharging phase (b) using experimental benchmarks from Al-Abidi et al. [39].

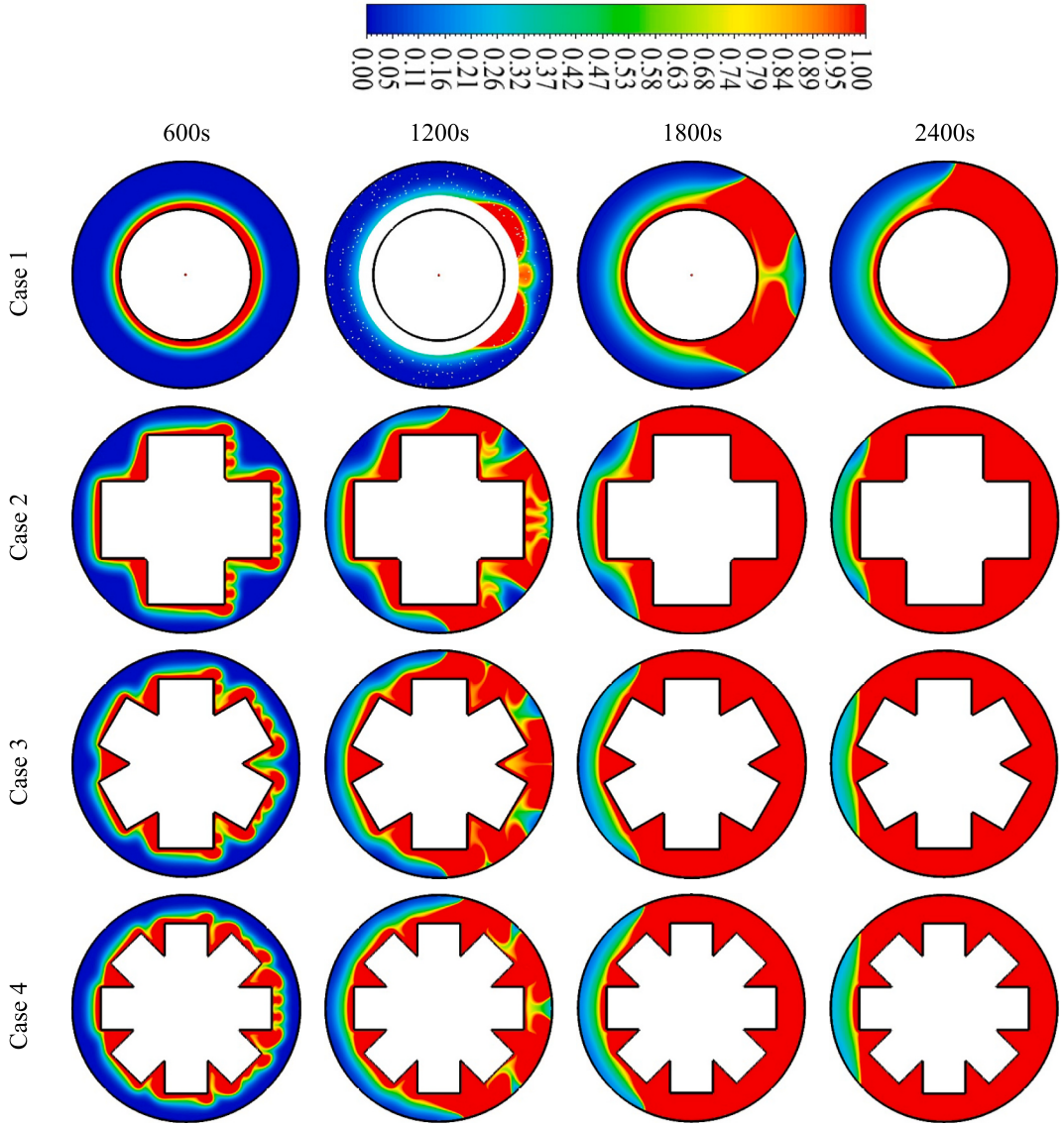


**Fig. 5.** Liquid fraction contours during PCM melting process for single-tube multi-lobed configurations (Cases 1–4) at different time intervals.

penetration zones that advance along the lobe extensions. The 4-lobe design (Case 2) creates four primary melting channels oriented at 90° intervals, resulting in a characteristic cross-shaped liquid region that provides enhanced thermal access to previously inaccessible PCM volumes. The liquid fraction distribution shows 15–20% melting completion compared to less than 10% for the baseline configuration at this early stage. The 6-lobe configuration (Case 3) exhibits superior thermal distribution characteristics, with six equally spaced melting fronts creating a more uniform liquid fraction field throughout the PCM domain. The reduced angular spacing between adjacent lobes (60° versus 90° for the 4-lobe design) promotes more effective thermal coverage within the PCM domain.

By 1200 s, Case 3 achieves approximately 70% liquid fraction with notably uniform distribution patterns, indicating an optimal balance between thermal penetration and lateral heat spreading. The 8-lobe design (Case 4) further increases the number of thermal penetration points but demonstrates only marginal improvements over the 6-lobe configuration. The reduced lobe width (15.18 mm versus 19.6 mm for Case 3) and closer angular spacing (45°) create more restricted flow channels that may limit the natural convection development within each lobe cavity. The liquid fraction contours at 1200 s show similar overall melting progress to Case 3, suggesting that the additional surface area

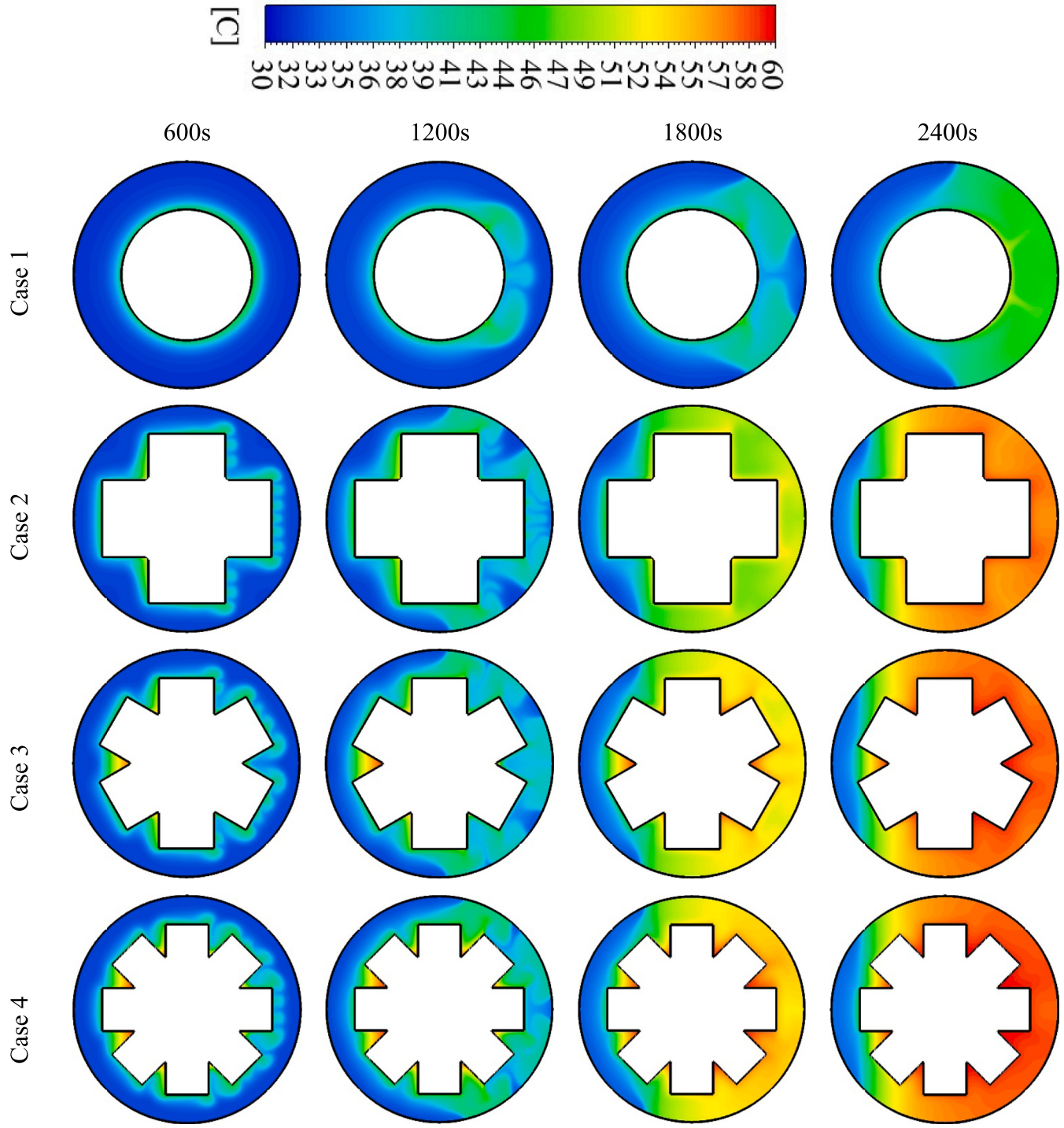


**Fig. 6.** Temperature contours during PCM melting process for single-tube multi-lobed configurations (Cases 1–4) at different time intervals.

provided by the eighth lobe pair is offset by reduced thermal effectiveness per unit surface area.

The progression to complete melting reveals distinct advantages of the multi-lobed geometries in the later stages of the process. At 1800 s, the baseline configuration shows significant solid PCM regions in the corners and periphery of the PCM domain, while the multi-lobed designs demonstrate nearly complete liquid fraction achievement, with only small solid regions persisting in the inter-lobe spaces. By 2400 s, the lobed configurations have achieved complete melting while the baseline case still retains approximately 35% solid fraction in the geometrically disadvantaged regions.

The temperature distribution patterns presented in Fig. 6 provide further evidence of enhanced thermal performance in the multi-lobed configurations. The temperature contours demonstrate that the lobed geometries create multiple high-temperature penetration zones that extend deeper into the PCM domain at all time intervals. The 4-lobe design (Case 2) creates four distinct thermal penetration zones with enhanced temperature fields extending along each lobe channel. The temperature distribution at 600 s shows elevated temperatures (50–55 °C) extending approximately 20–25 mm from each lobe tip, compared to similar temperature levels reaching only 10–15 mm from the circular tube surface. This enhanced thermal penetration directly correlates with accelerated melting rates and improved energy storage kinetics. Case 3 (6-lobe) demonstrates the most favorable temperature distribution characteristics among the evaluated configurations. The temperature contours reveal optimal thermal field overlap between adjacent lobes, creating continuous high-temperature regions that minimize cold spots and promote uniform melting progression. At 1200 s, the temperature field shows remarkable uniformity with over 80% of the PCM domain experiencing temperatures above 45 °C, compared to less than 60% for the baseline configuration. The 8-lobe configuration (Case 4) exhibits increased thermal surface area but demonstrates diminishing returns in thermal field enhancement. While the temperature contours show additional thermal penetration points, the individual lobe thermal development is somewhat restricted due to the reduced lobe dimensions and closer spacing. The thermal field overlap between adjacent lobes becomes more pronounced, potentially leading to thermal interference effects that limit the individual lobe effectiveness.

Quantitative analysis of the average liquid-fraction evolution in Fig. 7a confirms the superior melting kinetics of the multi-lobed designs. The liquid fraction progression shows that Cases 2, 3, and 4 achieve almost complete melting ($\lambda > 0.95$) in 2400 s compared to around 65% melting for the baseline configuration. Case 3 demonstrates the fastest melting rate, reaching 60% liquid fraction approximately 1200 s earlier than the baseline case. The mean temperature evolution in the mean temperature evolution (Fig. 7b) corroborates the liquid fraction findings and provides additional insights into the thermal energy absorption characteristics. The multi-lobed configurations maintain consistently higher average PCM temperatures throughout the melting process, with temperature advantages of 3–7 °C observed during the critical intermediate melting phase. Case 3 demonstrates the highest mean temperatures, reaching 40 °C approximately 800 s earlier than the baseline and maintaining temperature advantages throughout the process.

The heat storage rate comparison in Fig. 8 quantifies the most significant performance enhancement achieved through geometric modification. The multi-lobed configurations demonstrate heat storage rates ranging from 161.16 W to 164.04 W compared to 104.17 W for the baseline circular tube. Case 2 (4-lobe) achieves a 54.7% improvement with a heat storage rate of 161.16 W, while Cases 3 and 4 reach 164.04 W and 163.22 W respectively, corresponding to enhancements of 57.5% and 56.7%. The marginal performance difference between the 6-lobe and 8-lobe configurations, with less than 1% variation in heat storage rates, suggests that the optimal lobe number lies within the 6–8 range. The diminishing returns observed beyond six lobes indicate that additional surface area gains are offset by reduced thermal effectiveness per unit surface area and potential flow restrictions that limit heat transfer coefficient enhancement.

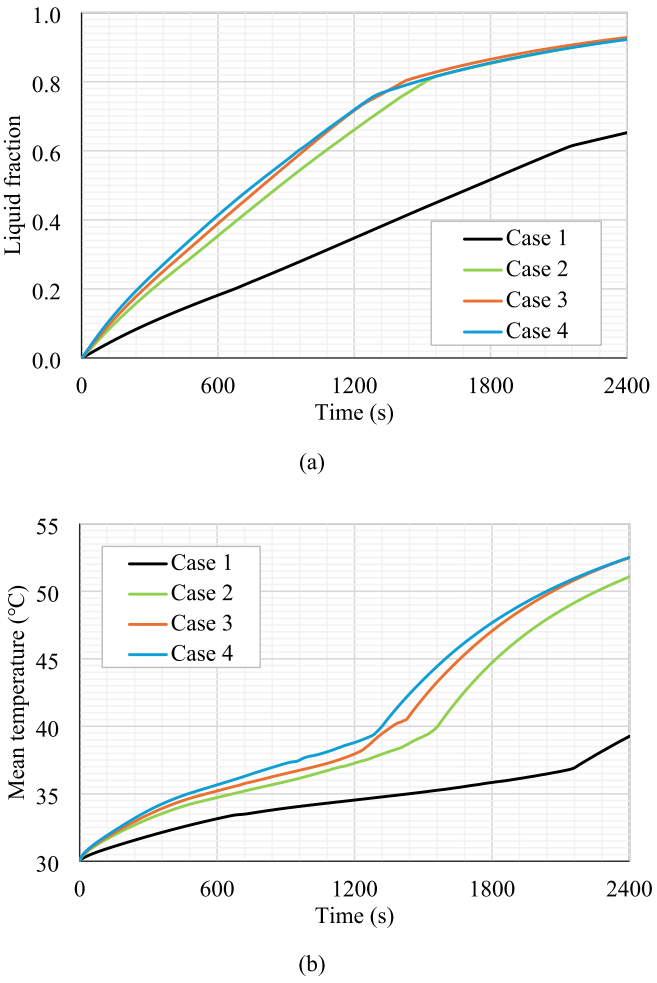


**Fig. 7.** Temporal evolution of (a) liquid fraction and (b) mean PCM temperature during melting for single-tube multi-lobed configurations (Cases 1–4).

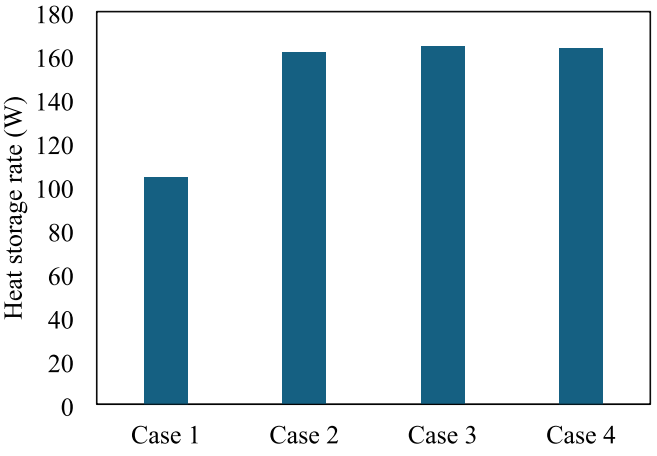


**Fig. 8.** Heat storage rates comparison for single-tube multi-lobed configurations (Cases 1–4) during the melting process.

The enhanced performance of multi-lobed configurations is attributed to several involving mechanisms. The increased heat transfer surface area directly enhances the thermal interaction between the heat transfer fluid and the PCM, while the lobe geometry creates localized thermal penetration pathways that accelerate the initial melting process.

The formation of multiple melting fronts promotes natural convection circulation patterns that distribute thermal energy more effectively throughout the PCM domain. Additionally, the geometric configuration influences the boundary layer development around each lobe, potentially enhancing local heat transfer coefficients through flow acceleration at the lobe tips.

### 5.1.2. Extended lobe configurations

The performance enhancement through geometric modifications extends beyond the determination of optimal lobe numbers to encompass the lobe extension length. This section analyzes Cases 4–6, specifically comparing the standard 8-lobe design with extended 8-lobe and deep-extension 8-lobe configurations. Three distinct configurations are considered: the standard 8-lobe design (Case 4) with 10 mm lobe extensions, the extended 8-lobe design (Case 5) featuring 12.5 mm extensions, and the deep-extension 8-lobe design (Case 6) incorporating 15 mm lobe extensions. The liquid-fraction contour maps presented in Fig. 9 reveal fundamental differences in melting progression patterns between these configurations. At 300 s, Case 6 exhibits localized liquid fraction values exceeding 0.8 at the lobe extremities, compared to maximum values of 0.6–0.7 observed in Cases 4 and 5.

The progression to intermediate melting stages (600–1200 s) demonstrates the cascading effects of enhanced thermal penetration. Case 6 develops continuous high liquid-fraction zones connecting adjacent lobe regions approximately 200 s earlier than Case 5 and 400 s earlier than Case 4. The liquid fraction distribution exhibits superior uniformity in Case 6, with minimal cold spots persisting in the inter-lobe regions. The enhanced thermal distribution is particularly evident at 1200 s, where Case 6 demonstrates liquid fraction values exceeding 0.9 throughout 80% of the PCM domain, compared to 65% for Case 5 and 50% for Case 4. The approach to complete melting (1800 s) reveals the cumulative advantages of deep lobe extensions. Case 6 achieves near-complete liquid fraction (>0.95) throughout the PCM domain while Cases 4 and 5 retain significant solid regions in the geometrically disadvantaged inter-lobe spaces. The melting front propagation in Case 6 demonstrates radial uniformity that approaches the ideal case, suggesting that the deep extension configuration effectively overcomes the geometric limitations inherent in multi-lobed designs.

The heat storage rate comparison (Fig. 10) quantifies the most significant performance enhancement metric for TES applications. Case 5 achieves a heat storage rate of 176.69 W compared to 163.22 W for Case 4, representing an 8.2% improvement that demonstrates the good benefits of moderate lobe extension. However, Case 6 achieves exceptional performance with a heat storage rate of 194.70 W, corresponding to a

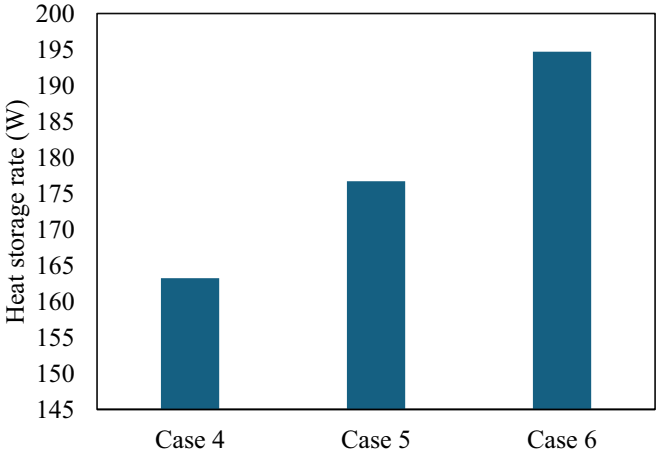


**Fig. 10.** Heat storage rates and melting time comparison for extended lobe configurations (Cases 4–6).

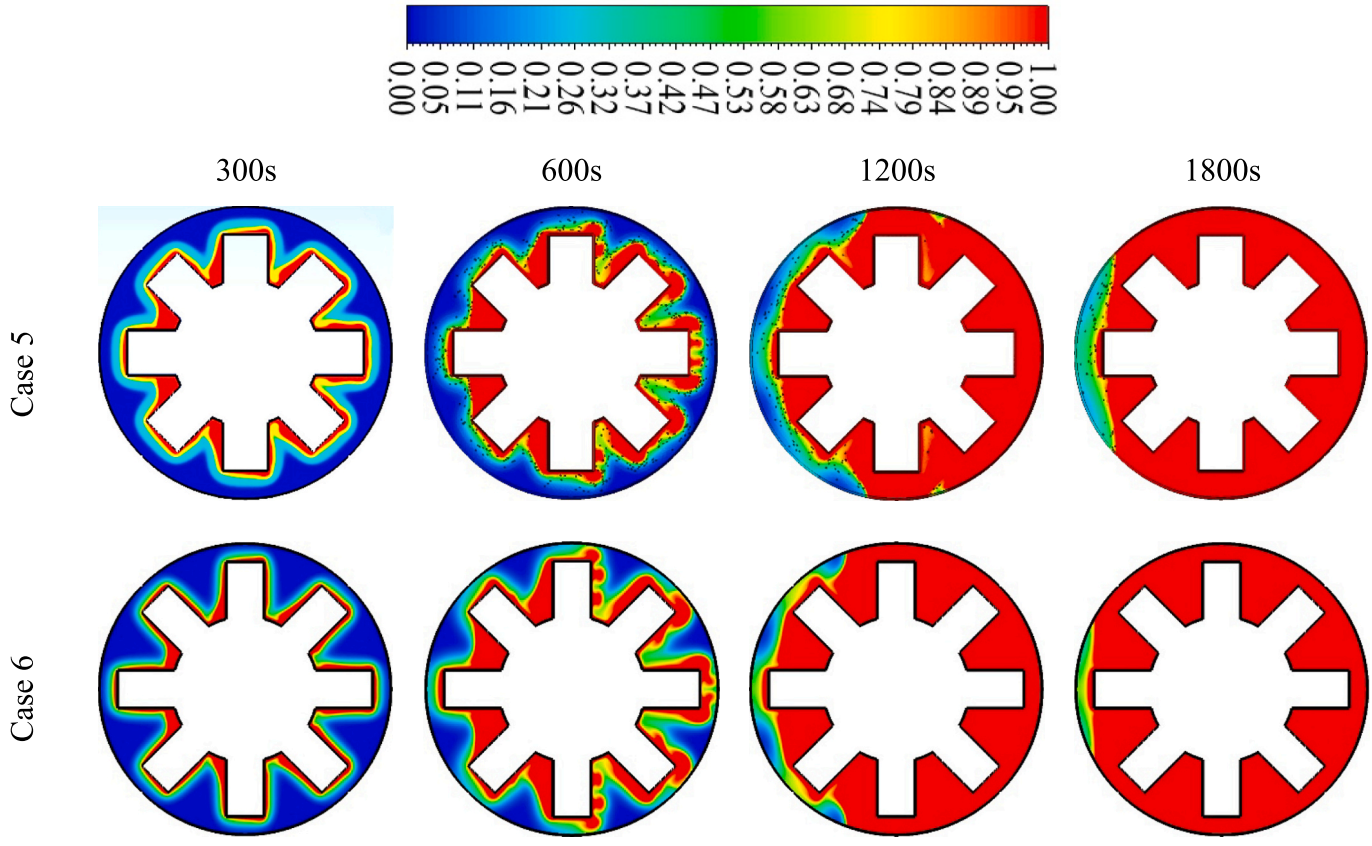


**Fig. 9.** Liquid fraction contours during PCM melting process for extended lobe configurations (Cases 5–6) at different time intervals.

19.3% enhancement over the standard 8-lobe design. This substantial improvement indicates that the 15 mm lobe extension length approaches optimal geometric proportions for the investigated system configuration. This enhancement in extended lobe configurations runs through multiple pathways. The increased heat transfer surface area provides direct enhancement to thermal interaction between the HTF and PCM, while the deeper thermal penetration reduces the effective thermal resistance to heat conduction within the PCM domain. Additionally, the extended lobe geometry influences local heat transfer coefficients through enhanced boundary layer development and potential flow acceleration effects at the lobe extremities.

### 5.1.3. Dual-tube connected configurations

The dual-tube connected configurations represent a new advancement in PCM-based system design, introducing cascaded heat transfer pathways through intermediate thermal zones that fundamentally alter the thermal interaction mechanisms between the HTF and the PCM. This section is to evaluate Cases 7–9, systematically comparing the dual-tube arrangements against the optimal single-tube configuration (Case 6). The dual-tube concept operates on the principle of thermal cascading, where heat transfer occurs through multiple sequential interfaces: from the primary HTF stream through the multi-lobed inner tube wall, into the intermediate PCM zone, and subsequently through the secondary tube wall into the outer PCM region. This configuration creates multiple thermal penetration pathways that simultaneously increase heat transfer surface area and promote enhanced thermal distribution throughout the PCM domain.

The liquid fraction evolution analysis, as illustrated in Fig. 11, reveals fundamental differences in melting progression patterns between the different dual-tube configurations. Case 7, featuring an 8-lobed primary tube connected to a 70 mm secondary tube, demonstrates exceptional melting kinetics with rapid liquid fraction development initiating simultaneously at both the primary lobe extremities and the secondary tube interface. At the initial 300 s interval, Case 7 exhibits liquid fraction values exceeding 0.8 in the primary thermal penetration zones and 0.6–0.7 in the secondary thermal regions, compared to maximum liquid fractions of 0.6 and 0.4 observed in Cases 8 and 9 respectively. The liquid fraction contours at 600 s reveal that Case 7 achieves near-complete melting (liquid fraction >0.9) throughout 70% of the PCM domain, while Cases 8 and 9 demonstrate complete melting coverage of 45% and 25% respectively. The enhanced thermal distribution in Case 7 is particularly evident in the intermediate PCM zones, where the thermal bridging between primary and secondary interfaces creates uniform melting progression that minimizes cold spots of single-

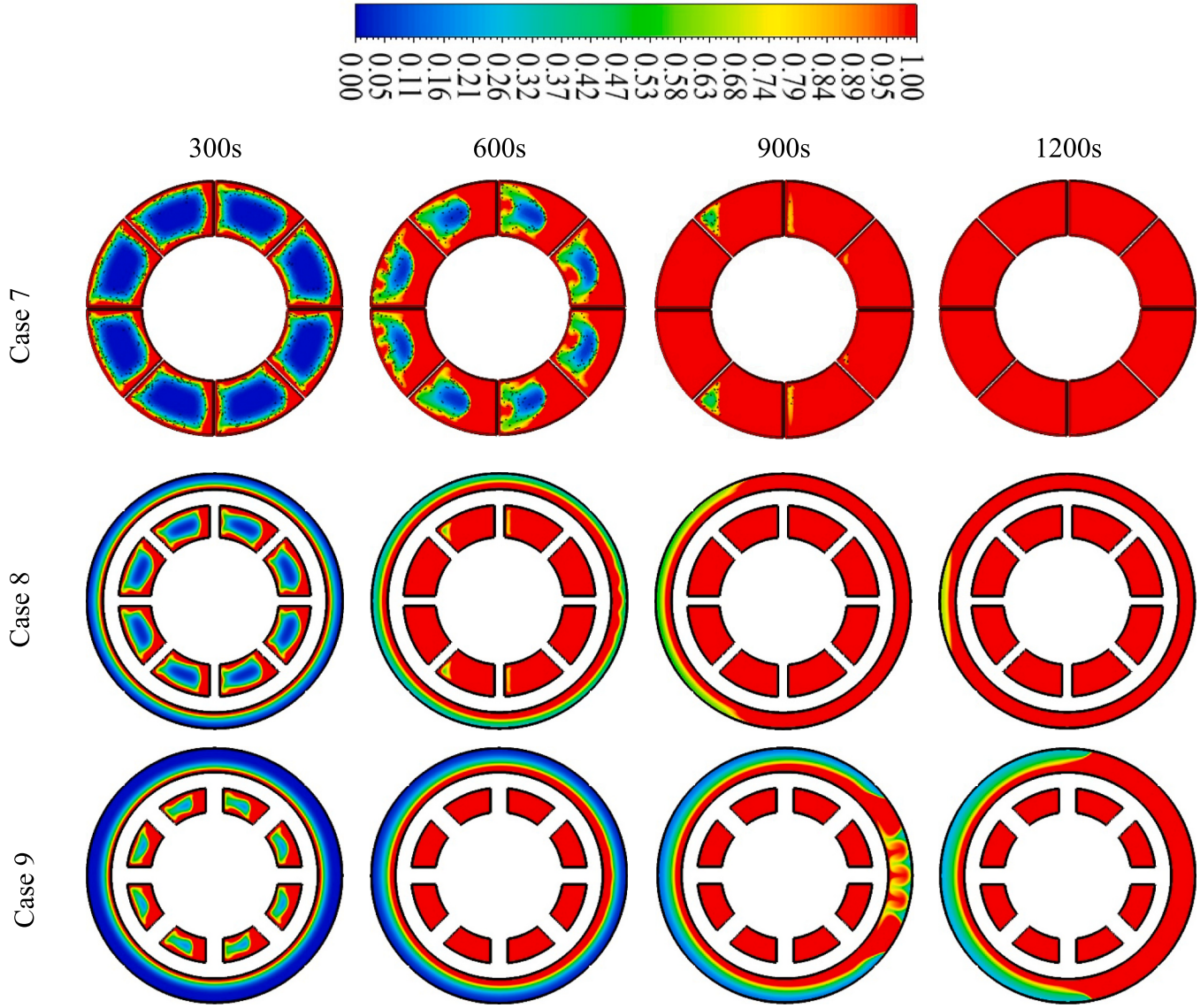


**Fig. 11.** Liquid fraction contours during PCM melting process for dual-tube connected configurations (Cases 7–9) at different time intervals.

tube configurations.

The approach to complete melting (1200s) reveals the cumulative advantages of optimal dual-tube geometric proportions. Case 7 achieves complete melting throughout the entire PCM domain while Cases 8 and 9 retain significant solid regions, particularly in the inter-connection zones and peripheral areas distant from both primary and secondary heat transfer interfaces. The melting front propagation in Case 7 demonstrates radial uniformity in thermal distribution, suggesting that the 70 mm secondary tube diameter with optimized connection geometry effectively overcomes the geometric limitations inherent in both single-tube and sub-optimal dual-tube designs.

The performance metrics comparison, quantified in Fig. 12, indicates that Case 7 achieves an exceptional heat storage rate of 419.39 W compared to 194.70 W for the optimal single-tube configuration, representing a remarkable 115.4% improvement. This substantial enhancement indicates that the 70 mm secondary tube diameter with optimized connection geometry approaches optimal geometric proportions for dual-tube PCM storage systems. Case 8 demonstrates significant performance enhancement with a heat storage rate of 303.73 W, corresponding to a 56.0% improvement over Case 6, while Case 9 exhibits degraded performance at 149.05 W, representing a 23.4% reduction compared to the single-tube benchmark.

These dual-tube performance enhancement mechanisms fundamentally alter the thermal interaction characteristics between the HTF and PCM. The increased heat transfer surface area provided by the secondary tube directly enhances thermal interaction capacity, while the intermediate thermal zone creates thermal buffering effects that promote more uniform temperature distribution throughout the PCM domain. The connection geometry influences local heat transfer coefficients through modified boundary layer development and potential flow acceleration effects, while the cascaded thermal pathways reduce effective thermal resistance through parallel heat transfer mechanisms. The optimal geometric proportions achieved in Case 7 demonstrate that dual-tube configurations can overcome the fundamental limitations of single-tube designs while maintaining the concentrated thermal penetration benefits of multi-lobed primary tube geometries.

### 5.2. Solidification performance analysis

#### 5.2.1. Single-tube multi-lobed configurations

The solidification performance analysis of single-tube multi-lobed configurations reveals fundamental differences in phase change kinetics. This section examines the baseline circular tube configuration (Case 1) against the modified geometries featuring 4-lobe (Case 2), 6-lobe (Case 3), and 8-lobe (Case 4) designs during the PCM discharging phase. The liquid fraction evolution contour maps presented in Fig. 13 demonstrate distinct solidification patterns that highlight the thermal advantages of multi-lobed geometries. The baseline configuration exhibits characteristic radially symmetric solidification that progresses slowly inward from the circular boundary, maintaining a relatively uniform solidification front throughout the discharging duration. The initial solidification phase (600 s) shows liquid fraction values exceeding 0.9 throughout the majority of the PCM domain. This slow solidification progression reflects the limited thermal extraction capacity inherent in circular tube geometries, where heat removal is constrained by the single thermal interface and the developing thermal boundary layer resistance. Meanwhile, the multi-lobed configurations create multiple thermal extraction pathways that fundamentally alter the solidification dynamics through preferential heat removal channels.

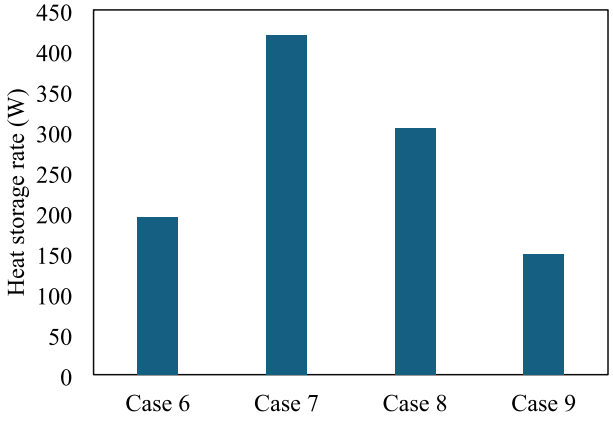


**Fig. 12.** Performance comparison of dual-tube connected configurations in terms of the heat storage rate (Cases 6–9).

The 4-lobe design (Case 2) establishes four primary solidification zones positioned at 90° intervals, forming distinct thermal extraction pathways that advance along each lobe extension into the PCM domain. At 600 s, the liquid fraction contours reveal localized solidification initiation at each lobe interface, with liquid fraction values dropping to 0.7–0.8 in the immediate vicinity of the lobe tips compared to values above 0.9 observed in the baseline configuration. The 6-lobe configuration (Case 3) demonstrates superior thermal extraction characteristics through its optimized geometric proportions. The reduced angular spacing between adjacent lobes (60° versus 90° for the 4-lobe design) promotes more effective thermal coverage within the PCM domain. The liquid fraction contours at 1200s show that Case 3 achieves approximately 50% solid fraction, compared to 35% solid fraction observed in Case 2 and less than 25% in the baseline configuration. The 8-lobe design (Case 4) achieves solidification kinetics comparable to Case 3, with complete solidification occurring within similar timeframes. The approach to complete solidification (2100–3300 s) reveals the cumulative thermal advantages of multi-lobed geometries in overcoming the geometric limitations of conventional circular designs. The multi-lobed configurations achieve nearly complete solidification while the baseline case retains significant liquid fractions in the central domain regions, demonstrating the effectiveness of multiple thermal extraction pathways in promoting uniform solidification progression throughout the PCM volume.

The temperature distribution contours presented in Fig. 14 provide complementary insights into the thermal field development mechanisms that drive the observed solidification enhancements. The multi-lobed configurations create multiple low-temperature penetration zones that extend deeper into the PCM domain at all time intervals, establishing enhanced thermal gradients that promote accelerated heat extraction. The 4-lobe design creates four distinct thermal extraction zones with enhanced low-temperature fields extending along each lobe channel, achieving temperature reductions to 15–20 °C extending approximately 20–25 mm from each lobe interface at 600 s, compared to similar temperature levels reaching only 10–15 mm from the circular tube surface in the baseline configuration. The 6-lobe configuration exhibits optimal temperature distribution characteristics among the evaluated designs, with temperature contours revealing superior thermal field overlap between adjacent lobes that creates continuous low-temperature regions throughout the PCM domain. At 1200s, the temperature field demonstrates remarkable uniformity with over 75% of the PCM domain experiencing temperatures below 25 °C, compared to less than 55% for the baseline configuration and 65% for the 4-lobe design. This enhanced thermal distribution reflects the optimal geometric proportions achieved in the 6-lobe configuration, where the lobe spacing and dimensions facilitate effective thermal extraction without creating thermal dead zones or geometric interference effects. The 8-lobe configuration demonstrates increased thermal extraction surface area but exhibits diminishing returns in thermal field enhancement effectiveness.

Quantitative analysis of the temporal evolution characteristics presented in Fig. 15 further confirm the thermal performance advantages of multi-lobed geometric modifications. The liquid fraction progression (Fig. 15a) demonstrates that Cases 2, 3, and 4 achieve complete solidification in approximately 2800–3000 s compared to 5400 s required for

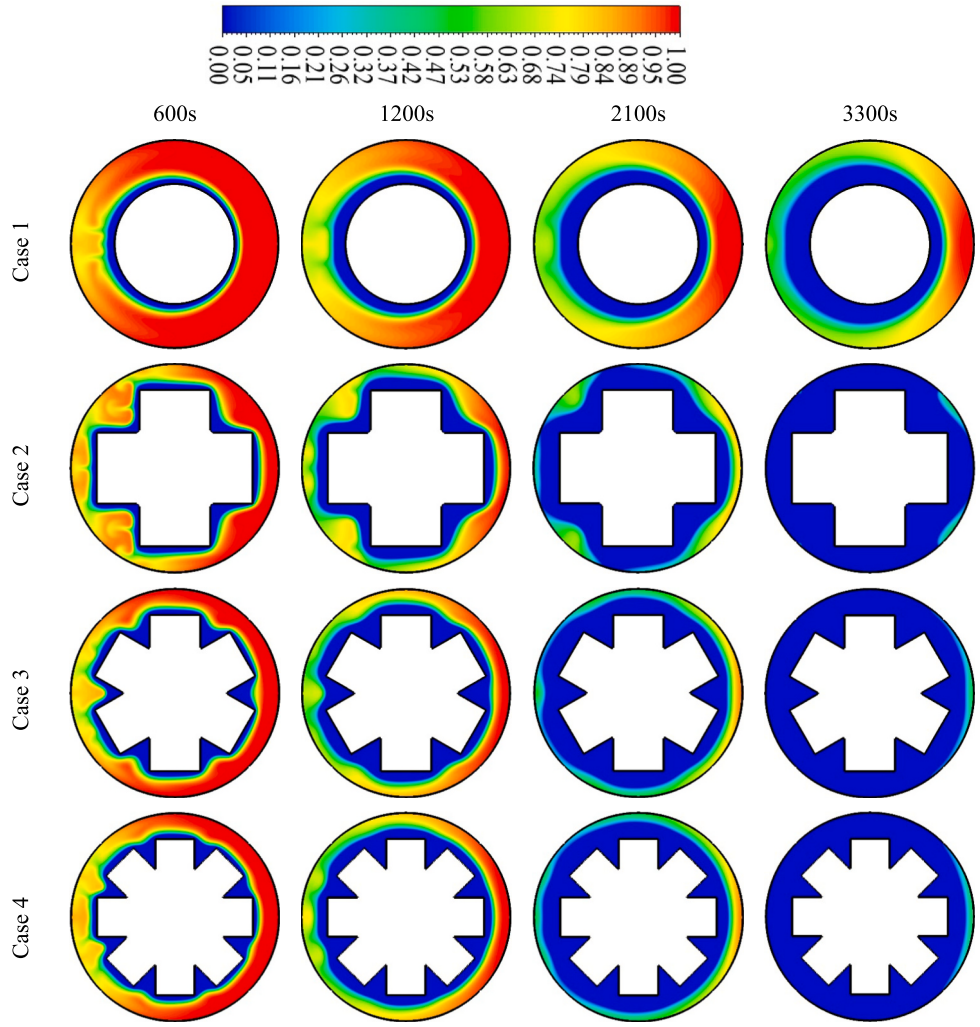


**Fig. 13.** Liquid fraction contours during PCM solidification process for single-tube multi-lobed configurations (Cases 1–4) at different time intervals.

the baseline configuration, representing solidification time reductions of 44–48%. The mean temperature evolution analysis (Fig. 15b) corroborates the liquid fraction findings while providing additional insights into the thermal energy release characteristics. The multi-lobed configurations maintain consistently lower average PCM temperatures throughout the solidification process, with temperature advantages of 2–5 °C observed during the critical intermediate solidification phase. These sustained temperature advantages indicate that the 6-lobe configuration achieves enhanced thermal coupling between the HTF and the PCM, reflecting reduced thermal resistance and improved heat transfer at the extraction interfaces.

The heat release rate comparison presented in Fig. 16 quantifies the substantial improvements in thermal power delivery capabilities by the multi-lobed configurations. They achieve heat release rates ranging from 119.88 W to 120.43 W compared to 68.80 W for the baseline case, representing remarkable improvements of 74–75% in thermal power extraction capacity. Case 2 achieves a heat release rate of 119.88 W, while Cases 3 and 4 demonstrate nearly identical performance at 120.19 W and 120.43 W respectively. The marginal performance difference between the 6-lobe and 8-lobe configurations, with less than 0.2% variation in heat release rates, provides strong evidence that optimal lobe density lies within the 6–8 range for the investigated system parameters. This provides design guidance for practical implementation of multi-lobed thermal energy storage systems.

### 5.2.2. *Extended lobe configurations*

This section analyzes Cases 4–6 during solidification, specifically comparing the standard 8-lobe design with extended 8-lobe and deep-extension 8-lobe configurations. The content examines how increasing lobe extension length impacts solidification performance and heat release capacity. The liquid fraction contour evolution presented in Fig. 17 demonstrates distinct solidification progression patterns that fundamentally differ from the melting characteristics observed in Section 5.1.2. The solidification process initiates simultaneously at all heat transfer surfaces, with solid formation progressing radially outward from the tube walls and lobe extremities. At 600 s, Case 6 exhibits solid fraction values (1-λ) exceeding 0.4 throughout 60% of the PCM domain, compared to 45% solid coverage in Case 5 and 30% in Case 4.

The intermediate solidification phase (1200–1800s) reveals the cascading effects of geometric enhancement on thermal energy extraction. Case 6 develops continuous solid regions connecting adjacent lobe zones approximately 300 s earlier than Case 5 and 600 s earlier than Case 4. At 1800 s, Case 6 demonstrates solid fraction values exceeding 0.8 throughout 75% of the PCM domain, compared to 60% for Case 5 and 45% for Case 4. The approach to complete solidification (2400 s) reveals the cumulative thermal performance advantages of deep lobe extensions. Case 6 achieves near-complete solidification (liquid fraction $<0.05$) throughout the PCM domain while Cases 4 and 5 retain significant liquid regions in the central core areas. The solidification front propagation in Case 6 demonstrates radial uniformity, suggesting that the 15 mm extension length effectively minimizes thermal resistance

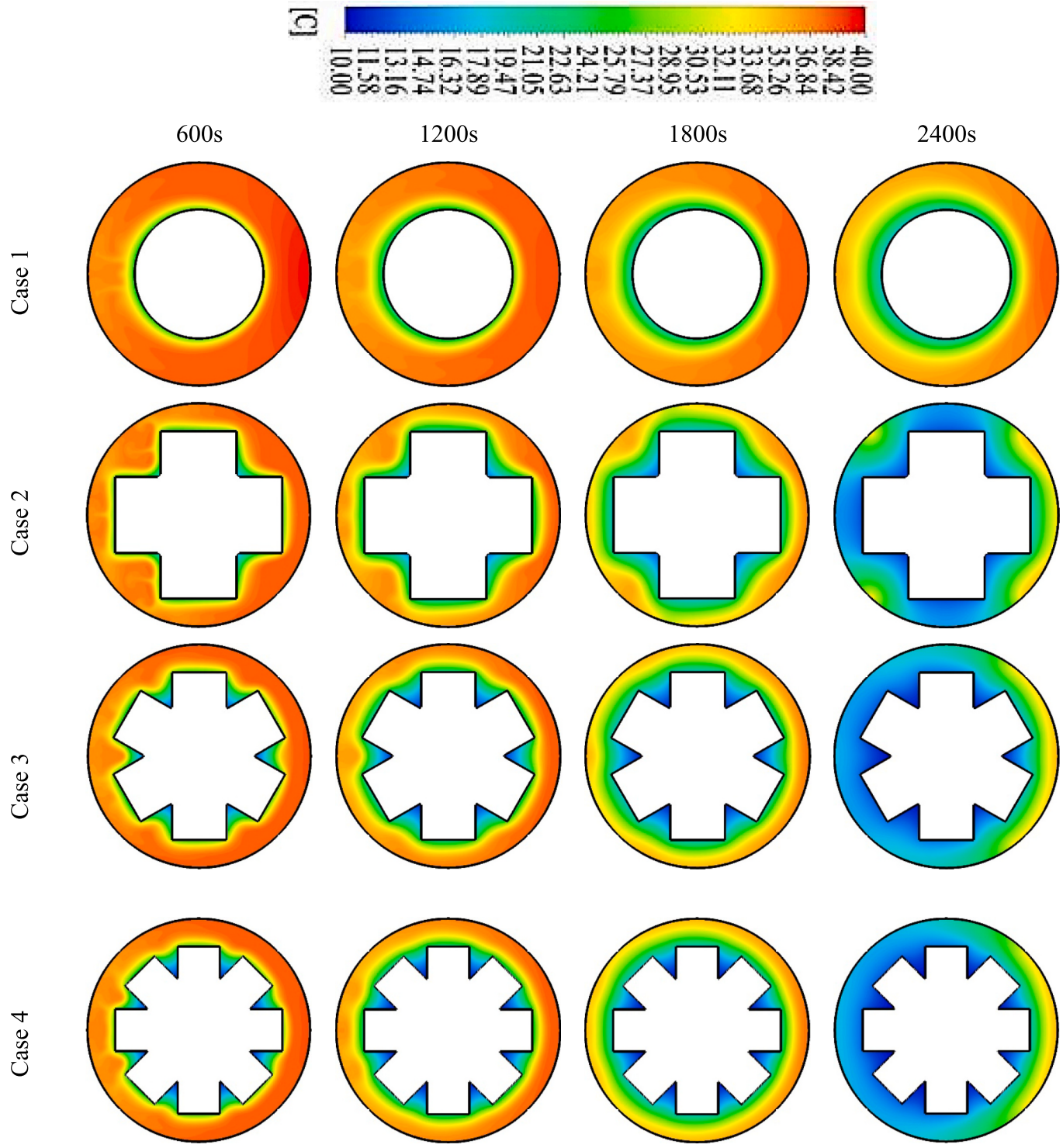


**Fig. 14.** Temperature contours during PCM solidification process for single-tube multi-lobed configurations (Cases 1–4) at different time intervals.

pathways during conduction-dominated heat transfer.

The heat release rate comparison quantified in Fig. 18 demonstrates the most significant performance enhancement metric for thermal energy storage applications during the discharging phase. Case 5 achieves a heat release rate of 152.14 W compared to 120.43 W for Case 4, representing a 26.3% improvement that demonstrates the substantial benefits of moderate lobe extension during solidification. However, Case 6 exhibits exceptional performance with a heat release rate of 189.16 W, corresponding to a 57.1% enhancement over the standard 8-lobe design and a 24.3% improvement over Case 5. The heat release rate enhancement observed in extended lobe configurations exceeds the corresponding improvements during melting (19.3% for Case 6), suggesting that geometric optimization provides greater relative benefits during solidification processes where natural convection effects are suppressed.

### *5.2.3. Dual-tube connected systems*

This section evaluates Cases 6–9 during the discharging phase, systematically comparing the optimal single-tube configuration (Case 6) with innovative dual-tube arrangements featuring varying secondary

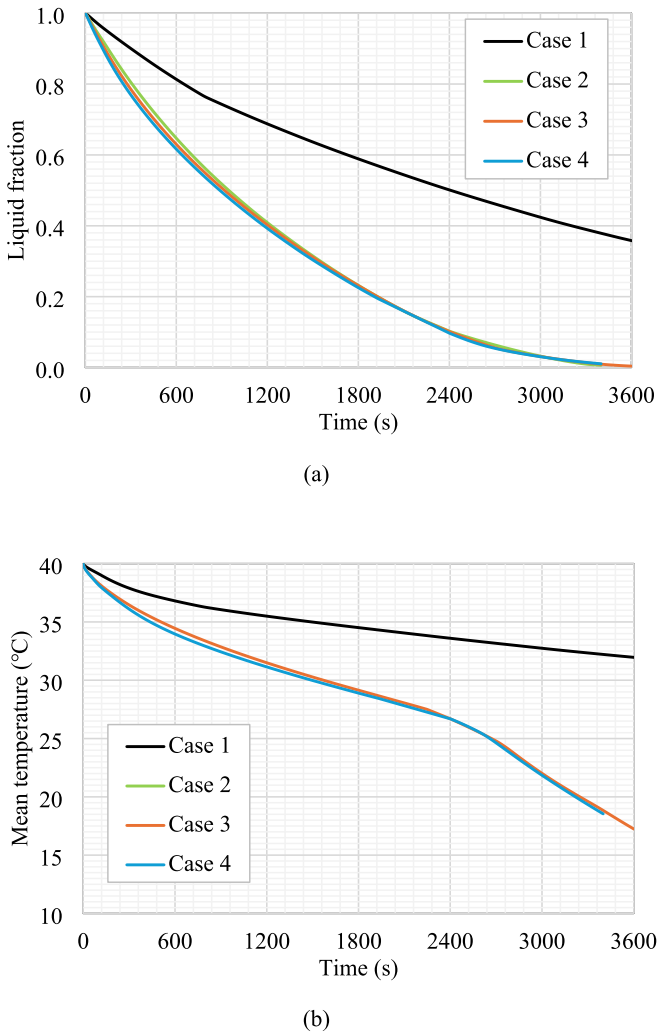


**Fig. 15.** Temporal evolution of (a) liquid fraction and (b) mean PCM temperature during solidification for single-tube multi-lobed configurations (Cases 1–4).

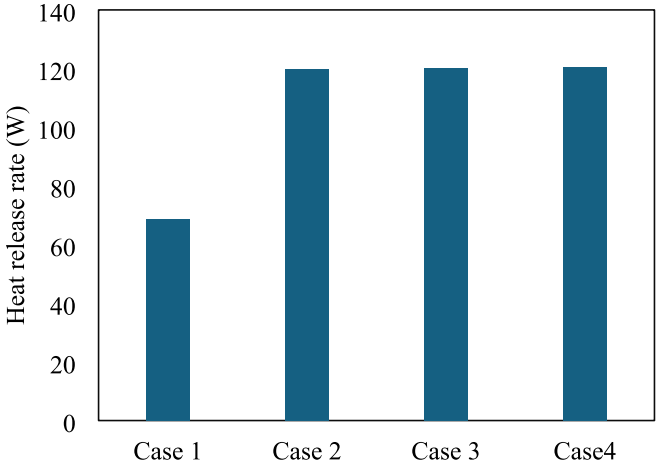


**Fig. 16.** Heat release rates comparison for single-tube multi-lobed configurations (Cases 1–4) during solidification process.

tube diameters. The liquid fraction evolution in Fig. 19 reveals fundamental differences in solidification progression patterns. Case 7, featuring an 8-lobed primary tube connected to a 70 mm secondary tube, demonstrates exceptional solidification kinetics with rapid solid fraction development at both primary lobe extremities and secondary tube interfaces. At the initial 300-s interval, Case 7 exhibits solid fraction values (1-λ) exceeding 0.3 throughout 65% of the PCM domain, compared to solid fraction coverage of 45% and 25% observed in Cases 8 and 9, respectively. During the intermediate solidification phase (600–900 s), Case 7 develops continuous solidification zones connecting primary and secondary thermal interfaces approximately 200 s earlier than Case 8 and 400 s earlier than Case 9.

The liquid fraction contours at 600 s reveal that Case 7 achieves solid fraction values exceeding 0.6 throughout 70% of the PCM domain, while Cases 8 and 9 demonstrate solid fraction coverage of 55% and 40%, respectively. Case 8, incorporating a 60 mm secondary tube diameter, exhibits superior performance characteristics that surpass even the optimized Case 7 configuration during the later stages of solidification. At 900 s, Case 8 demonstrates solid fraction values approaching 0.8 throughout 75% of the PCM domain, compared to 70% coverage in Case 7 and 50% in Case 9. This performance enhancement suggests that the 60 mm secondary tube diameter approaches optimal geometric proportions for maximizing heat extraction during conduction-dominated solidification processes. The approach to complete solidification (1200 s), Cases 7 and 8 achieve near-complete solidification (liquid fraction $<0.05$) throughout the entire PCM domain while Case 9 retains significant liquid regions, particularly in the peripheral areas distant from both primary and secondary heat transfer interfaces.

In Fig. 20, Case 8 attains an exceptional heat release rate of 401.54 W compared to 189.16 W for the optimal single-tube configuration, representing a remarkable 112.3% improvement in thermal power extraction capacity. The heat release rate enhancement observed in Case 8 significantly exceeds the corresponding improvement during melting (56.0%), providing strong evidence that dual-tube configurations offer greater relative benefits during discharging operations. Case 7 demonstrates a heat release rate of 354.28 W, corresponding to an 87.3% improvement over Case 6. Case 9 exhibits minimal performance enhancement at 193.43 W, representing only a 2.3% improvement over the single-tube benchmark. This implies that the optimal geometric proportions of dual-tube configurations in Cases 7 and 8 can overcome the fundamental limitations of single-tube designs during solidification while maintaining the enhanced thermal penetration benefits of multi-lobed primary tube geometries. The achieved advantages through Cases 7 and 8 provide important design guidance for practical implementation, suggesting that secondary tube diameter optimization within the 60–70 mm range can yield significant performance improvements.

## 6. Conclusions

This investigation has comprehensively examined the thermal performance enhancement of PCM thermal energy storage systems through advanced geometric modifications, encompassing single-tube multi-lobed configurations, extended lobe geometries, and innovative dual-tube connected systems. The numerical analysis, conducted using validated computational fluid dynamics modeling with the enthalpy-porosity method, has revealed fundamental insights into the thermal transport mechanisms governing PCM melting and solidification processes across nine distinct geometric configurations.

The evaluation of single-tube multi-lobed configurations has demonstrated that geometric optimization significantly enhances thermal performance compared to conventional circular tube designs. The 6-lobe configuration (Case 3) emerged as the optimal single-tube geometry, achieving a heat storage rate of (164.04 W vs 104.17 W) during melting and (120.19 W vs 68.8 W) during solidification, representing improvements of 57.5% and 74.8% respectively over the baseline circular configuration. The marginal performance difference between 6-lobe and 8-lobe configurations, with less than 1% variation in heat storage rates, established that optimal lobe density lies within the 6–8 range for the investigated system parameters.

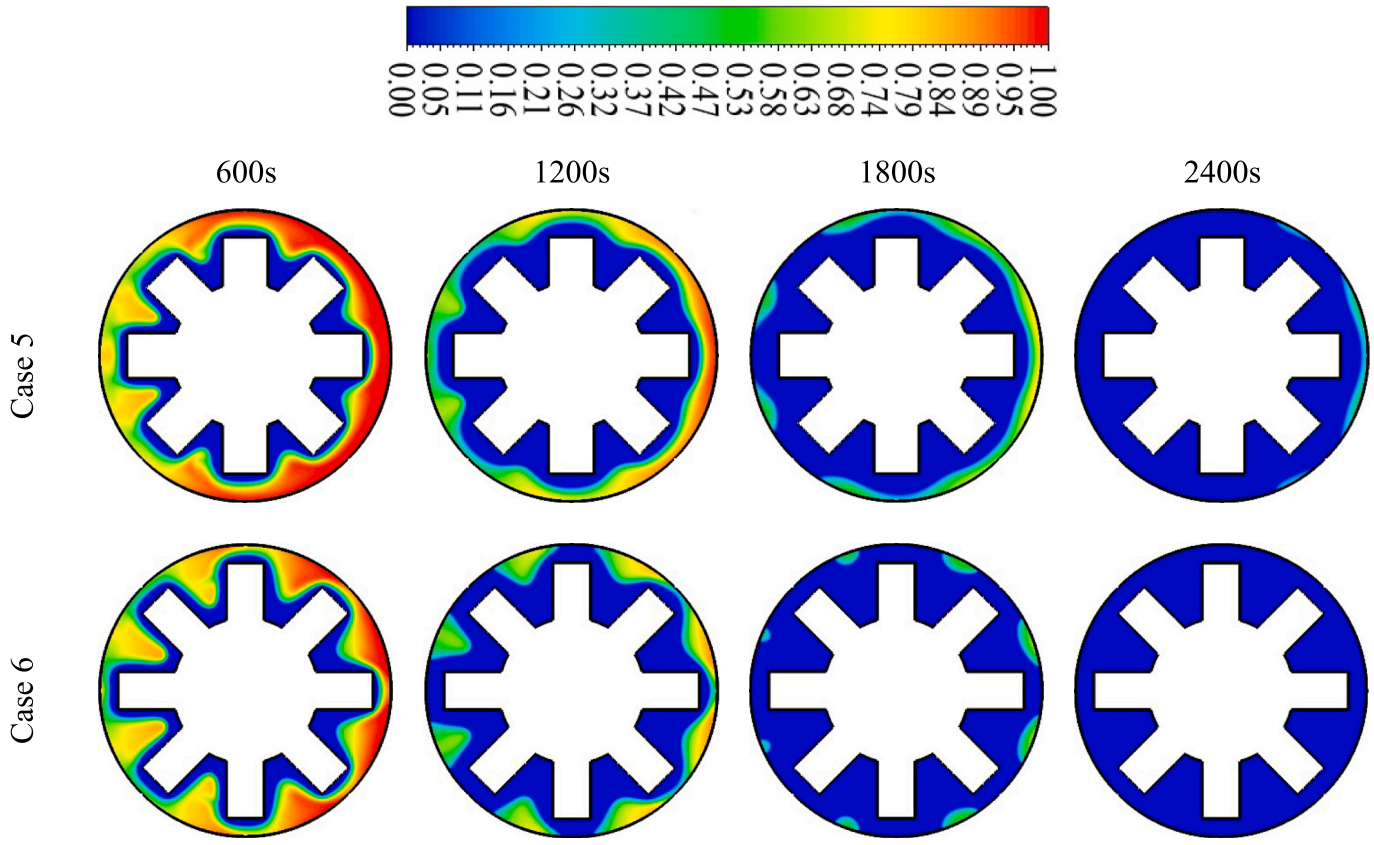


**Fig. 17.** Liquid fraction contours during PCM solidification process for extended lobe configurations (Cases 5–6) at different time intervals.

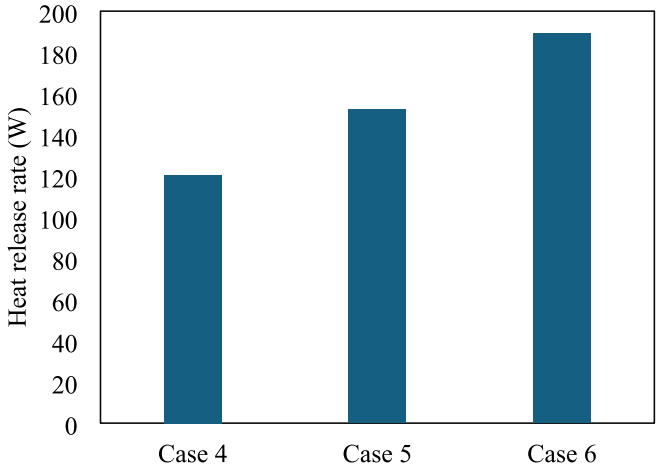


**Fig. 18.** Heat release rates comparison for extended lobe configurations (Cases 4–6) during solidification process.

The investigation of extended lobe configurations revealed that lobe extension length represents a critical design parameter that significantly influences thermal performance. The deep-extension 8-lobe configuration (Case 6) with 15 mm lobe extensions achieved exceptional performance with heat storage and release rates of 194.70 W and 189.16 W respectively, corresponding to 19.3% and 57.1% improvements over the standard 8-lobe design. The enhanced performance was attributed to deeper thermal penetration that reduces effective thermal resistance and creates more uniform temperature fields throughout the PCM domain.

The most significant advancement was achieved through the implementation of dual-tube connected configurations, which fundamentally altered the thermal transport mechanisms through cascaded heat transfer pathways and intermediate thermal zones. Case 8, featuring a 60 mm secondary tube diameter, demonstrated exceptional performance with heat storage and release rates of 303.73 W and 401.54 W respectively, representing improvements of 56.0% and 112.3% over the optimal single-tube configuration. The complete melting and solidification times were reduced by 35.4% and 53.5% respectively, with the solidification process showing greater relative improvement due to the effectiveness of multiple parallel thermal extraction pathways during conduction-limited transport.

From a practical implementation perspective, the investigation has established clear design guidelines for advanced PCM thermal energy storage systems. For applications requiring balanced charging and discharging performance, the 6-lobe configuration with 15 mm lobe extensions provides optimal single-tube performance with moderate complexity. For applications prioritizing maximum thermal performance, dual-tube configurations with secondary tube diameters in the 60–70 mm range offer exceptional performance enhancements that justify the additional system complexity. From a manufacturing perspective, the single-tube lobed profiles are producible through standard extrusion or drawing processes with minimal cost premium over conventional circular tubes. The dual-tube connected configurations require additional fabrication steps realizable through precision casting, hydroforming, or welded assembly, representing a moderate cost increase that is offset by the substantial performance improvements demonstrated. The reported enhancements are specific to RT-35 and the investigated shell diameter; their magnitudes will shift with PCM thermal conductivity, viscosity, and latent heat, and the specific preferred geometric values will change with system scale and aspect ratio. These are acknowledged as study limitations.

Future research should prioritize experimental validation of the proposed lobed and dual-tube configurations, which would identify any discrepancies arising from manufacturing tolerances or three-

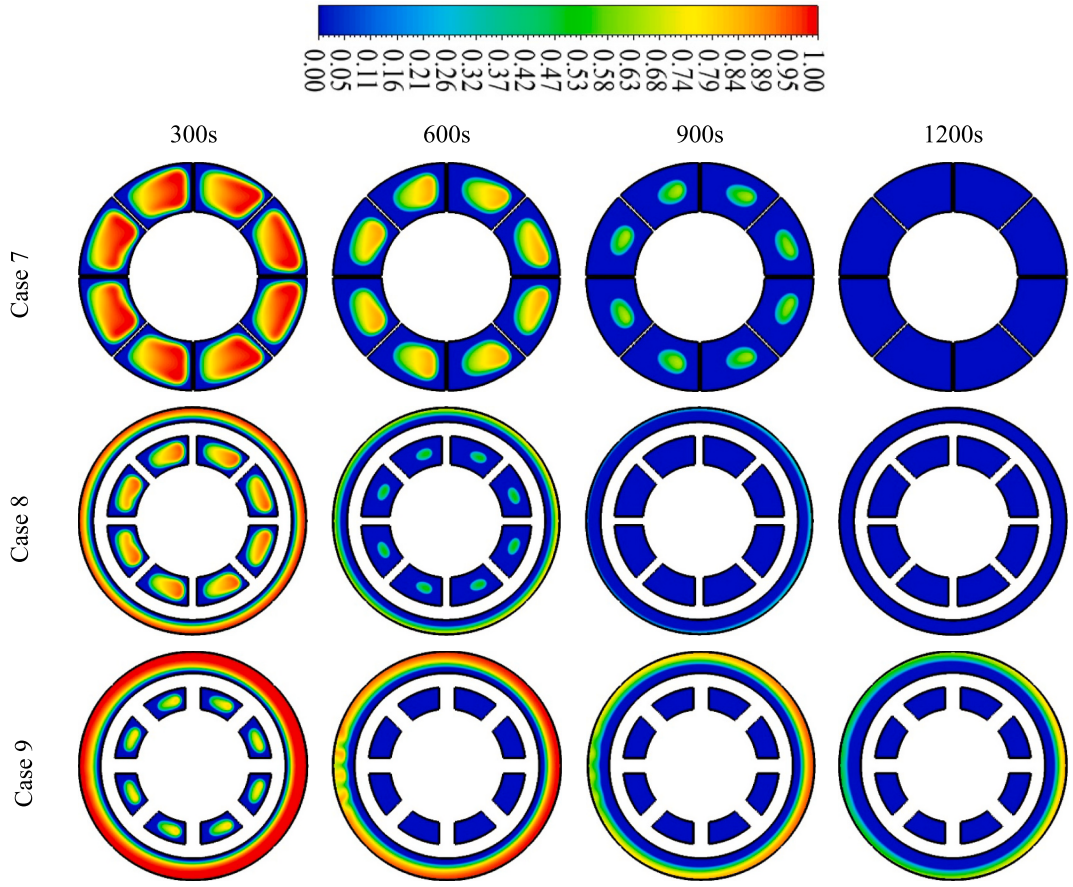


**Fig. 19.** Liquid fraction contours during PCM solidification process for dual-tube connected configurations (Cases 7–9) at different time intervals.

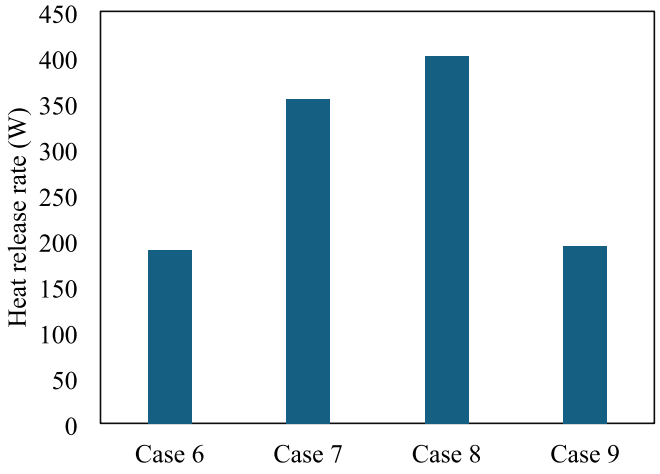


**Fig. 20.** Performance comparison of dual-tube connected configurations during solidification in terms of heat release rates (Cases 6–9).

dimensional flow effects. Extension to boundary conditions with realistic inlet temperature profiles representative of solar thermal and building applications would further quantify the sensitivity of the reported enhancement ratios to operating conditions. Thermal-hydraulic analysis of the dual-tube connected configurations incorporating pressure drop and pumping power penalties would complement the thermal benchmarks established here. Continuous optimization of lobe count and secondary tube diameter using response surface methodology would refine the preferred ranges identified here into rigorously optimized design parameters, and extension to inorganic PCMs, eutectics, and high-temperature salts is recommended to establish the generalizability of the design guidelines across PCM classes.

## CRediT authorship contribution statement

**Mhamed Benaissa:** Writing – review & editing, Writing – original draft, Visualization, Resources, Methodology, Investigation, Formal analysis, Conceptualization. **Nashmi H. Alrasheedi:** Writing – review & editing, Writing – original draft, Supervision, Methodology, Investigation, Funding acquisition, Formal analysis, Conceptualization. **Jasim M. Mahdi:** Writing – review & editing, Writing – original draft, Visualization, Validation, Resources, Project administration, Methodology, Formal analysis. **Hayder I. Mohammed:** Writing – review & editing, Writing – original draft, Visualization, Validation, Investigation, Formal analysis, Data curation, Conceptualization. **Khalil Hajlaoui:** Writing – review & editing, Writing – original draft, Resources, Methodology, Investigation, Formal analysis. **Mehdi Ghalambaz:** Writing – review & editing, Writing – original draft, Validation, Supervision, Software, Methodology, Investigation, Formal analysis, Conceptualization. **Mehdi Fteiti:** Writing – review & editing, Writing – original draft, Visualization, Validation, Resources, Methodology, Investigation, Formal analysis, Conceptualization. **Nidhal Ben Khedher:** Writing – review & editing, Writing – original draft, Software, Project administration, Formal analysis, Data curation.

## Funding

This work was supported and funded by the Deanship of Scientific Research at Imam Mohammad Ibn Saud Islamic University (IMSIU) (grant number IMSIU-DDRSP2603).

## Declaration of competing interest

The authors clarify that there is no conflict of interest for report.

## Acknowledgements

This work was supported and funded by the Deanship of Scientific Research at Imam Mohammad Ibn Saud Islamic University (IMSIU) (grant number IMSIU-DDRSP2603).

## Data availability

Data will be made available on request.

## References

[1] IEA, Renewables 2023, IEA, Paris, 2024. https://www.iea.org/reports/renewables-2023. in.
[2] IRENA, Innovation Outlook: Thermal Energy Storage, International Renewable Energy Agency, Abu Dhabi, 2020 in.
[3] L.F. Cabeza, Advances in thermal energy storage systems: Methods and applications, in: Advances in Thermal Energy Storage Systems, Elsevier, 2021, pp. 37–54.
[4] H. Nazir, M. Batool, F.J. Bolivar Osorio, M. Isaza-Ruiz, X. Xu, K. Vignarooban, P. Phelan, Inamuddin, A.M. Kannan, Recent developments in phase change materials for energy storage applications: a review, Int. J. Heat Mass Transf. 129 (2019) 491–523.
[5] H.M. Ali, T.-u. Rehman, M. Arıcı, Z. Said, B. Duraković, H.I. Mohammed, R. Kumar, M.K. Rathod, O. Buyukdagli, M. Teggar, Advances in thermal energy storage: fundamentals and applications, Prog. Energy Combust. Sci. 100 (2024) 101109.
[6] J. Kumar, P. Singh, R. Kumar, Advancement and challenges in latent heat thermal energy storage system, in: M. Muzammil, A. Chandra, P.K. Kankar, H. Kumar (Eds.), Recent Advances in Mechanical Engineering, Springer Singapore, Singapore, 2021, pp. 159–166.
[7] H. Sadiq, M. Mussa, Numerical study of thermal conductivity effect on the performance of thermal energy storage, J. Eng. 28 (2022) 57–77.
[8] S. Al Arni, H.S. Sultan Aljibori, A.M. Abed, H.I. Mohammed, J.M. Mahdi, H. Togun, A.M. Sadeq, M. Ghalambaz, N. Ben Khedher, Accelerated discharging kinetics in zigzag- shaped triplex-tube latent heat storage with nano-modified phase change materials additives, Case Stud. Therm. Eng. 70 (2025) 106140.
[9] H. Hosseininaveh, I.R. Abadi, O. Mohammadi, A. Khademi, M.B. Shafii, The impact of employing carbon nanotube and Fe3O4 nanoparticles along with intermediate boiling fluid to improve the discharge rate of phase change material, Appl. Therm. Eng. 215 (2022) 119032.
[10] N. Ajay Muraleedharan, W. Christopher, K. Babak, L. Jake, H. Ming Jun, G. Philip, J.H. Neil, Advancing Thermal Performance in PCM-Based Energy Storage: A Comparative Study with Fins, Expanded Graphite, and Combined Configurations, 2024.
[11] C. Zhao, M. Opolot, M. Liu, J. Wang, F. Bruno, S. Mancin, K. Hooman, Review of analytical studies of melting rate enhancement with fin and/or foam inserts, Appl. Therm. Eng. 207 (2022) 118154.
[12] M. Boujelbene, S.A. Mehryan, M. Sheremet, M. Shahabadi, N.B. Elbashir, M. Ghalambaz, Numerical study of a non-Newtonian phase change flow in finned rectangular enclosures, Facta Univ. Ser. Mech. Eng. 23 (2) (2024) 278–310.
[13] F. Alimi, K. Hajlaoui, M. Bouzidi, M. Mohamed, W. Yaïci, N.H. Alrasheedi, M. Ghalambaz, P. Talebidadehsardari, Charging and discharging heat transfer enhancement in a latent thermal energy storage array using petal-shaped tubes and fins, Case Stud. Therm. Eng. 74 (2025) 106917.
[14] M.A. Said, H.S. Sultan Aljibori, A.M. Abed, H. Togun, H.I. Mohammed, J.M. Mahdi, A. Rahbari, A.M. Sadeq, P. Talebizadehsardari, Innovative pipe profile configurations for fast charging of phase change material in compact thermal storage systems for building heating applications, Case Stud. Therm. Eng. 69 (2025) 106036.
[15] J.M. Mahdi, S. Lohrasbi, E.C. Nsofor, Hybrid heat transfer enhancement for latent-heat thermal energy storage systems: a review, Int. J. Heat Mass Transf. 137 (2019) 630–649.
[16] S.A.A. Mehrjardi, A. Khademi, M. Fazli, Optimization of a thermal energy storage system enhanced with fins using generative adversarial networks method, Therm. Sci. Eng. Prog. 49 (2024) 102471.
[17] S.A.A. Mehrjardi, A. Khademi, Z. Said, S. Ushak, A.J. Chamkha, Enhancing latent heat storage systems: the impact of PCM volumetric ratios on energy storage rates with auxiliary fluid assistance, Energy Nexus 11 (2023) 100227.
[18] A. Khademi, S.A.A. Mehrjardi, Z. Said, R. Saidur, S. Ushak, A.J. Chamkha, A comparative study of melting behavior of phase change material with direct fluid contact and container inclination, Energy Nexus 10 (2023) 100196.
[19] A. Khademi, S.A. Abtahi Mehrjardi, Z. Said, A.J. Chamkha, Heat transfer improvement in a thermal energy storage system using auxiliary fluid instead of Nano-PCM in an inclined enclosure: a comparative study, J. Appl. Comput. Mech. 9 (2023) 475–486.
[20] J. Kumar, P. Singh, R. Kumar, The effect of geometric parameters of a container on thermal charging of latent heat thermal energy storage system: A review, in: K. Govindan, H. Kumar, S. Yadav (Eds.), Advances in Mechanical and Materials Technology, Springer Nature Singapore, Singapore, 2022, pp. 1185–1195.
[21] F. Fornarelli, M. Valenzano, B. Fortunato, S.M. Camporeale, M. Torresi, P. Oresta, Heat transfer enhancement induced by the geometry of a LHTES device, Energy Procedia 148 (2018) 471–478.
[22] M. Kirincic, A. Trp, K. Lenic, J. Batista, Latent thermal energy storage performance enhancement through optimization of geometry parameters, Appl. Energy 365 (2024) 123255.
[23] N.B. Khedher, N. Biswas, H. Togun, H.I. Mohammed, J.M. Mahdi, R.K. Ibrahem, P. Talebizadehsardari, Geometry modification of a vertical shell-and-tube latent heat thermal energy storage system using a framed structure with different undulated shapes for the phase change material container during the melting process, J. Energy Storage 72 (2023) 108365.
[24] Y. Pahamli, M.J. Hosseini, A.A. Ranjbar, R. Bahrampoury, Inner pipe downward movement effect on melting of PCM in a double pipe heat exchanger, Appl. Math. Comput. 316 (2018) 30–42.
[25] S. Seddegh, X. Wang, M.M. Joybari, F. Haghighat, Investigation of the effect of geometric and operating parameters on thermal behavior of vertical shell-and-tube latent heat energy storage systems, Energy 137 (2017) 69–82.
[26] W. Ye, J.M. Khodadadi, Effects of varying geometrical parameters on the melting performance of phase change materials within L-shaped shell-and-tube latent heat thermal energy storage units with radial eccentricity exhibiting prominent influence, J. Energy Storage 86 (2024) 111334.
[27] J. Wołoszyn, K. Szopa, Shell shape influence on latent heat thermal energy storage performance during melting and solidification, Energies 16 (2023) 7822.
[28] A. NematpourKeshteli, M. Iasiello, G. Langella, N. Bianco, Thermal enhancement techniques for a lobed-double pipe PCM thermal storage system, Appl. Therm. Eng. 233 (2023) 121139.
[29] M. Fallah Najafabadi, H. Talebi Rostami, D.D. Ganji, Thermal and geometrical investigation of an original double-pipe helical coil heat storage system with Kock snowflake cross-section containing phase-change material, Appl. Therm. Eng. 226 (2023) 120244.
[30] M. Fallah Najafabadi, H. Talebi Rostami, M. Farhadi, Analysis of a twisted double-pipe heat exchanger with lobed cross-section as a novel heat storage unit for solar collectors using phase-change material, Int. Commun. Heat Mass Transf. 128 (2021) 105598.
[31] GmbH, Product Information, data sheet of RT35 by Rubitherm GmbH, in, https://www.rubitherm.eu/en/productcategory/organische-pcm-rt, 2026.
[32] P. Wang, X. Wang, Y. Huang, C. Li, Z. Peng, Y. Ding, Thermal energy charging behaviour of a heat exchange device with a zigzag plate configuration containing multi-phase-change-materials (m-PCMs), Appl. Energy 142 (2015) 328–336.
[33] N.B. Khedher, K. Hosseinzadeh, A.M. Abed, K. Khosravi, J.M. Mahdi, H.S. Sultan, H.I. Mohammed, P. Talebizadehsardari, Accelerated charging of PCM in coil heat exchangers via central return tube and inlet positioning: a 3D analysis, Int. Commun. Heat Mass Transf. 152 (2024) 107275.
[34] M. Esapour, M. Hosseini, A. Ranjbar, Y. Pahamli, R. Bahrampoury, Phase change in multi-tube heat exchangers, Renew. Energy 85 (2016) 1017–1025.
[35] S. Mat, A.A. Al-Abidi, K. Sopian, M.Y. Sulaiman, A.T. Mohammad, Enhance heat transfer for PCM melting in triplex tube with internal–external fins, Energy Convers. Manag. 74 (2013) 223–236.
[36] W.-B. Ye, D.-S. Zhu, N. Wang, Numerical simulation on phase-change thermal storage/release in a plate-fin unit, Appl. Therm. Eng. 31 (2011) 3871–3884.
[37] E. Assis, L. Katsman, G. Ziskind, R. Letan, Numerical and experimental study of melting in a spherical shell, Int. J. Heat Mass Transf. 50 (2007) 1790–1804.
[38] J. Vennard, Elementary Fluid Mechanics, 2007.
[39] A.A. Al-Abidi, S. Mat, K. Sopian, M.Y. Sulaiman, A.T. Mohammad, Experimental study of melting and solidification of PCM in a triplex tube heat exchanger with fins, Energy Buildings 68 (2014) 33–41.